

Technische Universität München  
Fakultät für Physik



**Master's Thesis in Physics (Nuclear, Particle, and Astrophysics)**

# **Fast Monte Carlo Simulation for Electron Scattering in the KATRIN Tritium Source**

**Schnelle Monte-Carlo-Simulation für Elektronenstreuung in der KATRIN  
Tritiumquelle**

Leo Laschinger

03 June 2024

Primary Reviewer: Prof. S. Mertens  
Secondary Reviewer: Prof. B. Märkisch  
Supervisors: Anthony Onillon, Korbinian Urban

# Contents

<b>Introduction</b>	<b>v</b>
<b>1 Neutrino Physics and Dark Matter</b>	<b>1</b>
1.1 Neutrino Discovery and Role in the Standard Model . . . . .	1
1.2 Neutrino Oscillations . . . . .	3
1.3 Neutrino Mass . . . . .	5
1.4 Sterile Neutrinos and Dark Matter . . . . .	7
<b>2 The KATRIN Experiment and the TRISTAN Project</b>	<b>11</b>
2.1 Measurement Principle . . . . .	11
2.2 KATRIN Experimental Setup . . . . .	12
2.3 TRISTAN - Search for keV-Scale Sterile Neutrinos . . . . .	21
<b>3 Electron Scattering on Gas Atoms and Molecules</b>	<b>29</b>
3.1 Introduction and Bethe Theory . . . . .	30
3.2 Total Cross Sections . . . . .	32
3.3 Elastic Scattering . . . . .	33
3.4 Electronic Excitation . . . . .	37
3.5 Ionization . . . . .	38
<b>4 Monte Carlo Simulations, Markov Chains and Random Number Generation</b>	<b>43</b>
4.1 Monte Carlo Principle and Random Numbers . . . . .	43
4.2 Sampling from a Distribution . . . . .	45
<b>5 Scattering Simulation</b>	<b>57</b>
5.1 General Working Principle . . . . .	57
5.2 Technical Details . . . . .	59
<b>6 Application and Results</b>	<b>67</b>
6.1 Source Simulation for TRISTAN . . . . .	67
6.2 KATRIN Energy Loss Investigations . . . . .	72
<b>7 Conclusion and Outlook</b>	<b>75</b>



# Introduction

The nature of Dark Matter (DM) is one of the biggest open questions in cosmology and particle physics. Matter in the universe is estimated to be composed of 84% DM, while "ordinary" matter (meaning particles contained in the Standard Model of Particle Physics (SM)) only accounts for 16% [1]. Even though the existence of DM is motivated by observations on many scales such as galaxy rotation curves, gravitational lensing, structure formation in the early universe and anisotropies in the Cosmic Microwave Background (CMB), its nature is still largely unclear. Promising particle candidates include Weakly Interacting Massive Particles (WIMPs), axions and sterile neutrinos [2].

Since DM particles would not (or hardly) interact with other particles via the fundamental forces, experimental detection is very challenging, regardless which candidate is considered. An opportunity to search for sterile neutrinos in the keV mass range is given by the KARlsruhe TRItium Neutrino (KATRIN) experiment. KATRIN is designed and currently operated for the measurement of the neutrino mass using beta spectroscopy from the decay of gaseous tritium. Latest results yield an upper limit on the neutrino mass of  $m_\nu < 0.8$  eV at 90% confidence level with a final sensitivity goal of  $< 0.3$  eV[3] <sup>1</sup>.

After the neutrino mass measurement is finished, technical modifications to the KATRIN beamline are planned in order to search for a keV scale sterile neutrino signal in the tritium spectrum. This project involves several new challenges compared to the neutrino mass measurement. While the latter investigated the endpoint of the tritium spectrum in an integral measurement, the keV sterile neutrino search will be performed using a differential measurement on almost the entire range of the tritium spectrum. This requires the development of a new detector, called TRISTAN, and a new data acquisition (DAQ) system capable of handling the very high rates that come with the increase of the energy range, but also a very accurate modelling of the experimental effects [4]. While the measurement of the neutrino mass is mainly limited by statistical uncertainty due to the low count rate at the spectrum endpoint, the search for a keV sterile neutrino is expected to be dominated by systematic uncertainties. Therefore, accurate modelling of the impact of the systematic effects and their uncertainties is required.

One of these effects is electron scattering in the tritium source. Electrons are pro-

---

<sup>1</sup>Here, as in the rest of this work, natural units ( $\hbar = c = e = 4\pi\epsilon_0 = 1$ ) are used unless otherwise specified, in order to simplify notation.

duced in the tritium gas via beta decay and first have to leave the source before being propagated to the detector. On their way through the gas, electrons can scatter on tritium molecules, changing their energy and direction. The purpose of this thesis was to develop a fast Monte Carlo simulation in order to accurately predict the impact of this effect.

Chapter 1 of this work will give a short overview on neutrino physics and dark matter, chapter 2 will introduce the KATRIN experiment and the TRISTAN project. The following chapters 3 and 4 will provide some theoretical background on scattering physics, Monte Carlo simulations and random number generation. The general structure and working principle of the simulation will be explained in chapter 5, while chapter 6 will focus on the results obtained with it. Finally, in chapter 7, a summary and outlook will be given.

# Chapter 1

## Neutrino Physics and Dark Matter

Neutrinos are sometimes also referred to as "ghost particles", because they interact so little with other particles. This makes them very hard to detect and experimentally investigate, resulting in their relatively late discovery compared to other particles of the SM. This chapter will give an overview over the most important aspects of neutrino physics. Section 1.1 will briefly outline the history of the discovery of the neutrino as well as its role in the SM. Neutrino oscillations will be explained in section 1.2. Their discovery was proof that neutrinos, contrary to prior belief, have a mass. The implications of this as well as attempts to measure the neutrino mass will be covered in section 1.3. Finally, section 1.4 will go beyond the SM and cover the hypothetical sterile neutrinos and especially their role as dark matter candidates.

### 1.1 Neutrino Discovery and Role in the Standard Model

The existence of neutrinos was first postulated by Wolfgang Pauli in 1930, in a letter addressed to the attendants of a conference on radioactivity [5]. It was Pauli's attempt at solving an important physics problem of the time: the beta decay was already known as a process where a nucleus decays and leaves behind a daughter nucleus and an electron (or positron). Since these were the only two outgoing particles that could be observed, the beta-decay was assumed to be a two-body decay. In this case, conservation of momentum and energy dictates that the outgoing electron's energy should be well defined. Histogramming the energy of beta electrons, a single line would be expected at a certain energy (or a set of lines close to each other, if one considers the excitation of the daughter nucleus).

However, what was observed was a continuous electron energy spectrum. This was a very puzzling result at the time and even led to physicists questioning the conservation of energy. Pauli however proposed the idea that a third, electrically neutral particle is emitted in the decay. In that case, the energy from the decay would be distributed randomly between the three decay products, leading to the observed continuous spectrum.

This idea was formalized a few years later by Enrico Fermi, who also coined the

term "neutrino" [6]. The decay can then be described in the following way:

$$n \rightarrow p + e^- + \bar{\nu}_e, \quad (1.1)$$

$$p \rightarrow n + e^+ + \nu_e, \quad (1.2)$$

where  $n$  represents a neutron,  $p$  a proton,  $e^-$  an electron and  $\bar{\nu}_e$  an electron anti-neutrino.

After the theoretical description by Fermi, it took about 20 years until the neutrino could be experimentally detected by Reines and Cowan in 1953 [7]. This was accomplished by observing the inverse beta decay,

$$\bar{\nu}_e + p \rightarrow n + e^+, \quad (1.3)$$

in a detector placed near a nuclear reactor. The capture of the neutron by the detector material and the annihilation of the positron with an electron produced a characteristic coincidence signal.

Two other kinds of neutrinos, corresponding to the two other charged leptons, muon  $\mu$  and tau  $\tau$ , were later also found. The muon neutrino  $\nu_\mu$  was discovered in 1962 by Danby et al. [8] by studying the decay of pions:

$$\pi^- \rightarrow \mu^- + \bar{\nu}_\mu, \quad (1.4)$$

$$\pi^+ \rightarrow \mu^+ + \nu_\mu. \quad (1.5)$$

The neutrinos from this decay produced muons via the inverse beta decay,

$$\bar{\nu}_\mu + p \rightarrow n + \mu^+, \quad (1.6)$$

$$\nu_\mu + n \rightarrow p + \mu^-, \quad (1.7)$$

but no electrons, which would happen via

$$\bar{\nu}_e + p \rightarrow n + e^+, \quad (1.8)$$

$$\nu_e + n \rightarrow p + e^-, \quad (1.9)$$

This led to the conclusion that muon neutrinos exist and are different particles than electron neutrinos.

In 2000, the tau neutrino was observed, again via the inverse decay

$$\bar{\nu}_\mu + p \rightarrow n + \mu^+, \quad (1.10)$$

$$\nu_\tau + n \rightarrow p + e^-, \quad (1.11)$$

by the Direct Observation of Nu Tau (DONUT) experiment [9]. The high energy neutrinos needed for that interaction were created by having 800 GeV protons collide

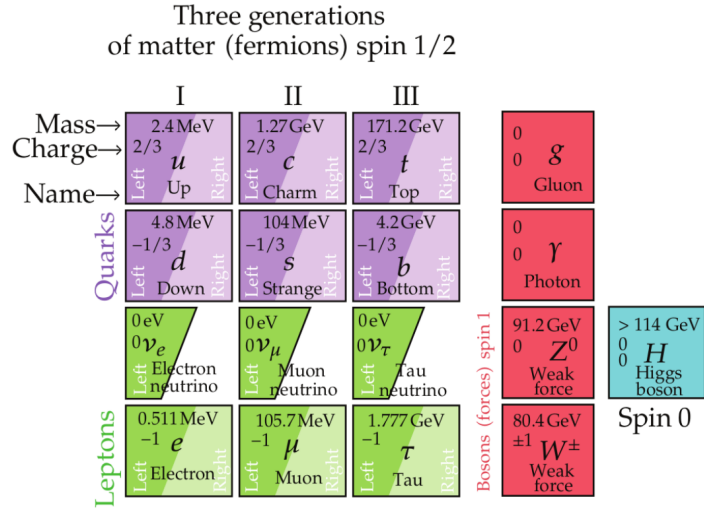


Figure 1.1: The Standard Model of Particle Physics including three generations of fermions, the force carrier bosons and the Higgs particle. As the weak interaction violates parity conservation, only left-handed neutrinos exist. In the SM, neutrinos are massless. Image adapted from [10].

with a tungsten target.

Today, neutrinos are established in the SM as leptons that carry neither electrical nor strong charge ("color") and thus only interact via the weak interaction. Figure 1.1 shows the SM including neutrinos.

Since the weak interaction maximally violates parity conservation, only left-handed neutrinos exist in the SM [11, 12]. This also means that neutrinos cannot have mass through the Higgs mechanism as the other SM particles, since the corresponding Lagrangian

$$\mathcal{L} \supset -m_\nu \nu_L^\dagger \nu_R - m_\nu \nu_R^\dagger \nu_L \quad (1.12)$$

requires a right-handed neutrino [13]. Therefore, neutrinos in the SM were initially assumed to be massless. However, the discovery of neutrino oscillations described in the next section proved that neutrinos in fact do have a mass, albeit a very small one.

## 1.2 Neutrino Oscillations

The first hint for neutrino oscillations was discovered observing the neutrino output of the sun in the Homestake experiment [14]. The flux of electron neutrinos was significantly lower than what was expected from the Standard Solar Model [15]. This

discrepancy was later confirmed by several other experiments [16–18]. A possible solution to this problem had already been published by Bruno Pontecorvo in 1957 [19]. His theory was then further developed into neutrino flavor mixing, which results in experimentally observable oscillations from one neutrino flavor into another [20].

This provides an explanation for the reduced flux of electron neutrinos from the sun. The oscillation theory could be proven by the SNO experiment, which showed that the solar neutrino flux matches the expectation when considering all 3 neutrino flavors [21]. Neutrino oscillations were then also observed on different length scales by several other experiments detecting neutrinos from the atmosphere, nuclear reactors and particle accelerators [22–24].

From a theoretical point of view, neutrino oscillations arise because the flavor eigenstates of the 3 neutrino generations ( $\nu_e$ ,  $\nu_\mu$  and  $\nu_\tau$ ) do not directly correspond to the 3 mass eigenstates (commonly labelled  $\nu_1$ ,  $\nu_2$  and  $\nu_3$ ), i.e. the solutions to the equation of motion in vacuum. Rather, the flavor eigenstates can be described as a quantum mechanical superposition of the mass eigenstates and vice versa. This relation is commonly described with the Pontecorvo-Maki-Nakagawa-Sakata matrix (PMNS matrix):

$$\begin{pmatrix} \nu_e \\ \nu_\mu \\ \nu_\tau \end{pmatrix} = \begin{pmatrix} U_{e1} & U_{e2} & U_{e3} \\ U_{\mu1} & U_{\mu2} & U_{\mu3} \\ U_{\tau1} & U_{\tau2} & U_{\tau3} \end{pmatrix} \begin{pmatrix} \nu_1 \\ \nu_2 \\ \nu_3 \end{pmatrix}, \quad (1.13)$$

in which the matrix elements  $U_{ij}$  depend on 3 mixing angles  $\theta_{12}$ ,  $\theta_{13}$ ,  $\theta_{23}$  and a complex phase  $\delta$ . Since neutrinos only interact weakly, their creation and detection corresponds to a measurement of the flavor state resulting in a *collapse* of the wave function into one of the flavor eigenstates. However, their propagation corresponds to the mass eigenstates, which, as described by equation (1.13) are a linear combination of the flavor eigenstates. As a result, there is a non-zero probability that upon arrival of the neutrino, a different flavor state is measured than at its creation. In the simplified case of only two neutrinos, this oscillation probability is described by:

$$P(\nu_a \rightarrow \nu_b) = \sin^2(2\theta) \sin^2\left(\frac{L}{4E} \Delta m^2\right), \quad (1.14)$$

and thus depends on the mixing angle  $\theta$ , the propagation length  $L$ , the energy  $E$  and the difference of the squared masses  $\Delta m^2 = m_1^2 - m_2^2$  [13].

From this equation, it can clearly be seen that at least 2 of the 3 neutrinos cannot be massless, since in that case the oscillation probability would vanish. This fact of course immediately prompts the question on the value of the neutrino masses. Possible theoretical explanations for the neutrino mass as well as experimental efforts to measure it will be covered in the next section.

### 1.3 Neutrino Mass

As established in the previous sections, neutrinos have a mass, but not via the same mechanism as the other particles in the SM, described by equation (1.12). Some possible alternative theoretical descriptions of the neutrino mass will be briefly outlined in the following.

One approach to theoretically explain neutrino masses is to assume they are Majorana particles, i.e. their own antiparticles. This is possible and consistent with the restrictions of the SM since neutrinos do not carry electric charge. The neutrino could then have a so-called Majorana mass introduced by a Lagrangian of the form

$$\mathcal{L} \supset -\frac{m_\nu}{2} \left( \nu_L^T \epsilon \nu_L - \nu_L^\dagger \epsilon \nu_L^* \right) \quad (1.15)$$

with  $\epsilon = \begin{pmatrix} 0 & 1 \\ 1 & 0 \end{pmatrix}$ , which would eliminate the need for a right-handed neutrino [13].

One possible way to test if this occurs in nature is through the rare double-beta decay. In certain unstable atoms, single beta decay is forbidden by energy conservation, but two nucleons can decay at once in a so-called double beta decay (here e.g. for two neutrons being converted to protons, increasing the proton number  $Z$  by 2 while the total number of nucleons  $A$  stays constant):

$$(Z, A) \rightarrow (Z + 2, A) + 2e^- + 2\bar{\nu}_e. \quad (1.16)$$

If the neutrino is indeed its own antiparticle, the two neutrinos could annihilate in the decay, resulting in the so-called Neutrinoless Double Beta Decay ( $0\nu\beta\beta$ ):

$$(Z, A) \rightarrow (Z + 2, A) + 2e^-. \quad (1.17)$$

Extensive experimental search for this decay has been performed in the past and further experiments are also planned for the future [25]. So far, no signal has been observed. The current leading half-time limit for the  $0\nu\beta\beta$  by the GERDA experiment is  $T_{1/2} > 1.8 \times 10^{26}$  s at 90% confidence level [26, 27].

Other approaches to explain the neutrino mass assume the existence of a right-handed neutrino. Due to the parity violation of the weak interaction, this neutrino would not even interact weakly, leading to the name *sterile neutrino*, which will be covered in more detail in the next section. The existence of this neutrino would then allow for a Higgs-mass as described in equation (1.12) just as the other particles in the SM. However, in that case, in order to explain the small mass of the neutrino, the coupling constant to the Higgs field would have to be a lot smaller than that of all the other particles, which seems arbitrary. This led to the development of another possible solution involving right-handed neutrinos, called the seesaw mechanism.

In brief, in the seesaw mechanism the existence of a right-handed neutrino is assumed

and all allowed terms of the Lagrangian are considered. This includes Majorana mass terms  $m_{L,R}$  along with the "regular" Dirac mass  $m_D$  from the Higgs term:

$$\mathcal{L} \supset \frac{1}{2} \left[ m_D (\bar{\nu}_L N_R + \bar{N}_L^c \nu_R^c) + m_L \bar{\nu}_L \nu_R^c + m_R \bar{N}_L^c N_R \right], \quad (1.18)$$

where  $\nu$  denotes the active and  $N$  the sterile neutrino [28]. If now one considers a case where  $m_L = 0$  (i.e. the active neutrino is not a Majorana particle) and  $m_R \gg m_D$ , one can calculate the following mass eigenvalues for the active and sterile neutrino:

$$m_\nu = \frac{m_D^2}{m_R},$$

$$m_N = m_R \left( 1 + \frac{m_D^2}{m_R^2} \right) \approx m_R.$$

This means that the larger the sterile/Majorana mass is, the smaller the active neutrino mass is. This relationship explains the smallness of the active neutrino mass and is the origin of the name *seesaw* for this mechanism. Depending on the details of the theory, a very large range of masses is possible for the sterile neutrino, reaching from  $\mathcal{O}(100 \text{ MeV})$  to  $\mathcal{O}(10^{15} \text{ GeV})$  [29, 30].

Regardless of the theoretical description, the value of the neutrino mass is of great interest. There are many different experiments trying to determine it using various different methods, several of which will be briefly mentioned in the following.

If one assumes the neutrino to be a Majorana particle, the half-life limit on the  $0\nu\beta\beta$  from the GERDA experiment can be converted into a limit of

$$m_{\beta\beta} = \left| \sum_{i=0}^3 U_{ei}^2 e^{i\alpha_i} m_i \right| < (79 - 180) \text{ meV}$$

at 90% confidence level on the so-called coherent sum of the neutrino mass states (which contains complex Majorana phases  $\alpha_i$ ) [27]. This limit is compatible with those from other  $0\nu\beta\beta$  experiments [27].

Observations of the CMB by the Planck satellite so far also did not detect any effects of the neutrino mass and can thus pose a limit of

$$\sum_{i=0}^3 m_i < 0.39 \text{ eV}$$

on the sum of the neutrino masses. This limit can be tightened to

$$\sum_{i=0}^3 m_i < 0.11 \text{ eV}$$

if gravitational lensing and baryonic acoustic oscillation data are also taken into account [1].

While the  $0\nu\beta\beta$  approach makes a strong assumption on the nature of the neutrino, the neutrino mass determination through observation of the CMB relies heavily on the cosmological model employed. While current models mostly make valid predictions, there are also discrepancies with other experimental data, which are most notable in the difference between the Planck CMB result for the Hubble constant and that of other experiments with a tension  $> 5\sigma$  [31].

A model-independent way of measuring the neutrino mass is given by beta spectroscopy. Here, the kinematics of the outgoing electron in a beta decay (as described by equation (1.1)) are studied in detail, which allows conclusions on the neutrino mass. The KATRIN experiment currently provides the most stringent beta spectroscopy limit on the neutrino mass of

$$m_\beta = \sqrt{\sum_{i=1}^3 U_{ei}^2 m_i^2} < 0.8 \text{ eV}$$

at 90% confidence level on the incoherent sum of the neutrino masses [3]. The experiment will be explained in detail in chapter 2.

With the seesaw mechanism, this section provided a first motivation for the existence of sterile neutrinos. Other problems that could be solved by the existence of sterile neutrinos as well as some theoretical background will be discussed in the next section.

## 1.4 Sterile Neutrinos and Dark Matter

As already mentioned in the introduction, the universe contains about 84% non-interacting matter of unknown nature, called Dark Matter (DM). This is a conclusion formed in order to explain effects on many scales such as the velocity at which galaxies rotate, gravitational lensing effects, the velocity dispersion in galaxy clusters, the way structures have been formed in the early universe, and temperature anisotropies of the CMB [2]. Although theories exist to explain these effects by modifying the theory of gravity [31], assuming the existence of a previously unknown non-interacting particle seems the most straightforward solution to solve these issues. This is additionally supported by the observation of the bullet cluster effect that provides strong evidence for the particular character of DM [32].

Concerning the nature of these particles, many theories exist such as supersymmetric particles, extra-dimensional particles, axions and sterile neutrinos [2], the latter of which will be explained in more detail here.

While in principle, any lepton that does not carry any charge could be considered a sterile neutrino, introducing sterile right-handed neutrinos is arguably the most



questions.

An eV mass scale sterile neutrino could explain anomalies observed in many short baseline oscillation experiments [33–36]. The corresponding parameter space is currently being tested, among others by the KATRIN experiment, but so far no sterile neutrino was found [37].

As already mentioned in the previous section, a heavy sterile neutrino with a mass of 100 MeV to  $10^{15}$  GeV could provide an explanation for the existence as well as the smallness of neutrino masses via the seesaw mechanism. These neutrinos could only be detected by production in accelerators. Any natural abundance would have to have decayed before the Big Bang Nucleosynthesis, since otherwise the abundance of light elements would be different than what is observed today [38].

As a potential DM particle, sterile neutrinos on the keV mass scale are attractive candidates. Depending on the production mechanism, they could be so-called warm DM, and as such resolve potential issues with the common cold DM models such as the amount of satellite dwarf galaxies and the density distribution of galaxy cores [39]. Several X-ray telescopes have detected an excess line at an energy of 3.5 keV, which could potentially indicate the presence of a sterile neutrino with a mass of 7 keV [40, 41]. However, this result is controversial and hints exist that point against a sterile neutrino signal [42].

A search for the signal of a keV-scale sterile neutrino in the tritium spectrum will be performed in the KATRIN experiment, after the current neutrino mass measurement is finished. The measurement principle and technical setup of the KATRIN neutrino mass measurement as well as modifications made for the sterile neutrino search will be explained in the following chapter.



## Chapter 2

# The KATRIN Experiment and the TRISTAN Project

The Karlsruhe TRItium Neutrino (KATRIN) experiment has been designed and is currently operating to measure the mass of the neutrino with a sensitivity goal of  $< 0.3 \text{ eV}$ . Latest results yield an upper limit of  $m_\beta < 0.8 \text{ eV}$  at 90% confidence level [3]. KATRIN measures the energy spectrum of electrons emitted near the endpoint of the tritium beta decay. This is done through an integral measurement, where only electrons above a variable threshold are counted by a detector. Due to the small region around the endpoint that is investigated, count rates at the detector are low ( $\mathcal{O}(1 \text{ events/s})$ ), and the KATRIN neutrino mass measurement is planned to take data until 2026 for a total of about 1000 days in order to lower statistical uncertainties enough to achieve the design sensitivity [43].

For the keV sterile search, which will extend the measurement far deeper into the spectrum, a differential measurement with much higher count rates will be performed. This requires several technical modifications to the beamline, as well as accurate modelling of the systematic effects, which become more important compared to the statistical uncertainties [4].

Section 2.1 in this chapter will explain the general principle of the KATRIN neutrino mass measurement. Section 2.2 will go into a little more detail on the experimental setup. Unless otherwise noted, information in there will be based on the KATRIN Technical Design Report [43]. Section 2.3 will explain the measurement principle of the keV sterile neutrino search along with the necessary technical modifications to the KATRIN beamline as well as a short overview on the most important systematic effects. The latest KATRIN results will be shown in section 2.2.7

### 2.1 Measurement Principle

The KATRIN experiment attempts to measure the neutrino mass by studying the beta decay of tritium to helium-3:



Tritium was chosen due to its short lifetime of 12.3 y, resulting in a high activity, and its relatively low energy endpoint of 18.6 keV [3]. Since the  $T_2$  molecule is much heavier than the electron and the antineutrino, the latter two divide almost all the energy from the decay among them as kinetic energy. However, since the neutrino needs to at least receive the amount of energy it has through its rest mass, the maximum possible energy for the electron depends on the neutrino mass value. That means that the neutrino mass slightly distorts the endpoint of the electron spectrum, as illustrated in figure 2.1.

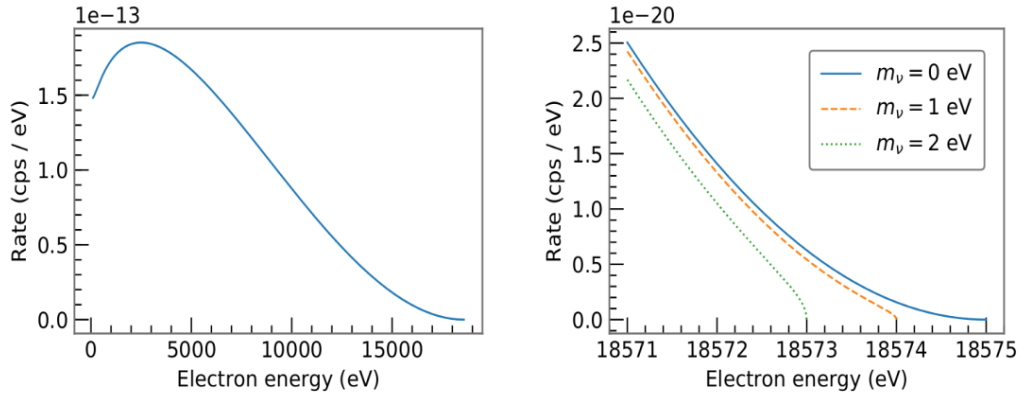


Figure 2.1: Energy spectrum of electrons from tritium decay (left) and distortions of the spectrum endpoint induced by a neutrino mass of 1 and 2 eV, for illustration purposes (right). Image from [44].

Essentially, the goal of the KATRIN experiment is to measure the energy spectrum around the endpoint to a degree of precision high enough to infer the neutrino mass. This is done through an integral measurement, where the high resolution spectrometer, a Magnetic Adiabatic Collimation combined with an Electrostatic Filter (MAC-E Filter), filters out all electrons below a certain threshold energy. Only electrons with a higher energy can pass the spectrometer and are then counted at the detector. The threshold energy is varied around the endpoint and the change in countrate observed. This can then be compared to a theoretical prediction of the spectrum in order to get information on the neutrino mass.

## 2.2 KATRIN Experimental Setup

This section will give an overview over the KATRIN experimental setup and its most relevant components. Figure 2.2 shows an illustration of the beamline.

Electrons are produced in the Windowless Gaseous Tritium Source (WGTS) (sec-

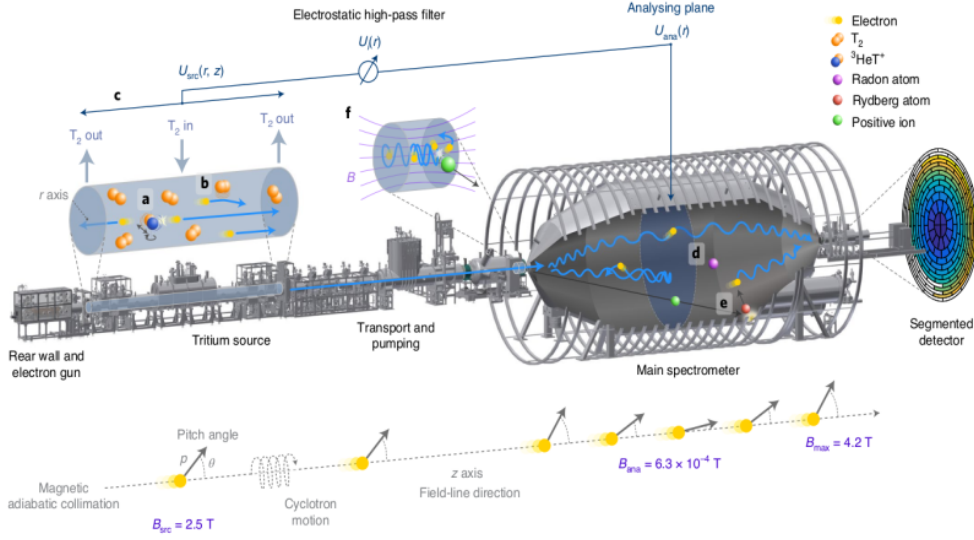


Figure 2.2: Illustration of the KATRIN setup. Electrons are produced in the tritium source and are guided by magnetic fields towards the detector. In the pumping section, the tritium flow is reduced by 14 orders of magnitude. In the main spectrometer, electrons below the threshold energy are filtered out. Finally, the detector counts the electrons that pass the main spectrometer. On the left, the setup is terminated by the Rear Wall. Figure from [3].

tion 2.2.1) and then guided towards the spectrometer by magnetic fields. On the other side, the beamline is terminated by the rear section, covered in section 2.2.2. In the pumping section, the tritium molecules are removed from the beam (section 2.2.3) in order to preserve an ultra-high vacuum at the spectrometer, where all electrons below the threshold energy are filtered out (section 2.2.4). The remaining electrons then arrive at the detector, covered in section 2.2.5. Finally, section 2.2.6 will provide a short overview on the response function of the beamline.

### 2.2.1 Windowless Gaseous Tritium Source

The Windowless Gaseous Tritium Source (WGTS) consists of a steel tube of 10 m length and 90 mm diameter. Tritium gas of purity  $>95\%$  is circulated in a closed loop by injecting it in the center of the source and pumping it out at both ends. Figure 2.3 shows a schematic of the WGTS as well as the approximate density profile.

The nominal column density of the tritium gas is  $\rho d = 5 \times 10^{17}$  molecules/cm<sup>2</sup>, resulting in an activity of  $1.7 \times 10^{11}$  Bq. The gas is kept at a temperature of 30 K in order to reduce Doppler broadening through the thermal motion of the molecules

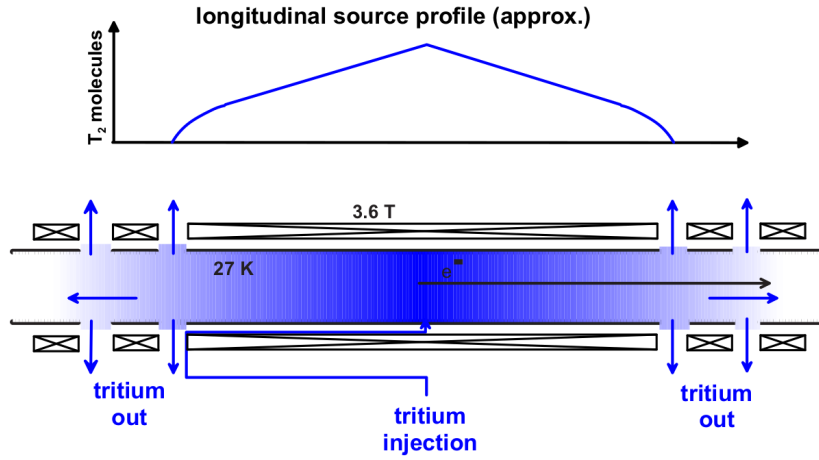


Figure 2.3: Visualization of the WGTS setup, as well as an approximate tritium density distribution (top). Low-temperature tritium is injected into the middle and drifts towards the ends, where it is pumped out. Figure from [43].

and to maintain the high tritium density at a relatively low pressure [3]. Both the temperature and the column density are kept stable to a precision below 0.1 %/h. The beam tube is surrounded by superconducting magnets generating a magnetic field strength of 3.6 T to guide the electrons either to the rear wall or to the pumping and transport section, covered in the next sections.

### 2.2.2 Rear Section

The rear section houses the Calibration and Monitoring System (CMS), which comprises an electron gun as well as the possibility to install radioactive calibration sources. These can be used to perform measurements concerning the transmission function (see section 2.2.6) and other calibration measurements. The CMS is shielded from tritium flow by a differential pumping section. The beamline is terminated by a gold-plated rear wall on a small bias voltage, which defines the electric potential of the WGTS.

### 2.2.3 Pumping Section

In the pumping and transport section, the tritium flux is reduced to below  $10^{-14}$  mbar · l/s in order to avoid background by decaying tritium molecules in the spectrometer section. This is achieved by two pumping systems: the Differential Pumping Section (DPS) and the Cryogenic Pumping Section (CPS).

The DPS consists of five beam tubes tilted by 20° with respect to each other to

prevent tritium molecules from travelling from the WGTS to the spectrometers in a straight line. Four turbomolecular pumps removing the tritium molecules result in a reduction of tritium flux by a factor of about  $10^7$  in the DPS.

The remaining flux reduction happens then in the CPS, again by about seven orders of magnitude. Here, six tubes, again tilted by  $20^\circ$ , have their surface covered with a helium-cooled argon frost layer which captures nearly all of the rest of the tritium molecules.

### 2.2.4 Pre- and Main Spectrometer

The spectrometer section consists of the pre- and the main spectrometer. Both operate on the MAC-E Filter principle, visualized in figure 2.4.

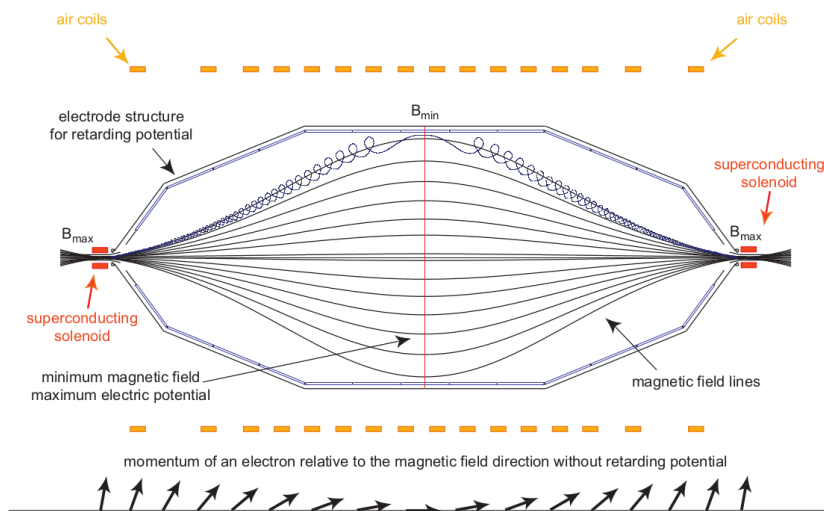


Figure 2.4: Schematic drawing of the KATRIN main spectrometer as an illustration of the MAC-E Filter principle. From the source side to the center, the magnetic field is drastically reduced in order to convert any electron momentum transversal to the beamline into longitudinal momentum, as illustrated by the black arrows. That way, more electrons with enough total energy can overcome the electrostatic potential and do not get rejected due to their initial direction. Figure from [45].

Electrons arrive at the spectrometers in a cyclotron motion induced by the guiding magnetic fields. The angle of their momentum vector towards the beamline, called the *pitch angle*, determines how the momentum of the electrons is divided between transversal movement towards the detector and cyclotron movement.

The basic idea of the spectrometers is to apply an electrostatic potential to only let electrons above a certain energy threshold pass to the detector. However, only

electron momentum parallel to the beamline plays a role in overcoming that potential, any transversal momentum in the form of a cyclotron motion does not. To overcome this in order to increase the yield of electrons, the magnetic field between the entrance (and exit) and the center of the spectrometer is reduced by about 4 orders of magnitude, from several Tesla to  $3 \times 10^{-4}$  T. This causes the cyclotron radius of the electrons to drastically increase, and transversal momentum to be converted into longitudinal momentum. The energy resolution of the MAC-E Filter is then determined by the remaining transversal momentum, which depends on the minimum and maximum magnetic field applied:

$$\Delta E = E \cdot \frac{B_{\min}}{B_{\max}}. \quad (2.2)$$

The KATRIN design energy resolution is 0.93 eV at the tritium endpoint, using a maximum magnetic field of  $B_{\max} \approx 6$  T [46].

For the latest results of the neutrino mass measurement, the pre-spectrometer is operated at 10 keV electrostatic potential in order to reduce the flux of electrons already before the main spectrometer [3]. Figure 2.5 shows a visualization of the electric and magnetic field strength along the beamline. At the main spectrometer, there is a drastic drop of the magnetic field to a minimum value of  $B_{\min} = B_{\text{ana}} \approx 3 \times 10^{-4}$  T followed by a sharp increase to a maximum field strength  $B_{\max}$ . At the same location as the drop of the magnetic field, the electric potential sharply increases to filter out electrons below the threshold energy.

The main spectrometer has a length of 23.38 m and a maximum diameter of 9.8 m in order to accommodate the large electron cyclotron radii. This results in a volume of about  $1400 \text{ m}^3$  that is kept at an ultra-high vacuum of  $10^{-11}$  mbar.

The maximum initial angle towards the beamline an electron can have and still be transmitted to the detector is determined by the ratio of the magnetic fields at the entrance (i.e. on the source side,  $B_{\text{src}}$ ) and the exit (maximal value of the magnetic field,  $B_{\max}$ ):

$$\theta_{\max} = \arcsin \left( \sqrt{\frac{B_{\text{src}}}{B_{\max}}} \right). \quad (2.3)$$

In current KATRIN operation,  $\theta_{\max} = 50.4^\circ$  [3].

Electrons that have an energy above the electrostatic potential and an initial angle below the acceptance angle are transmitted to the detector, which is covered in the next section.

## 2.2.5 Detector

The electrons that are transmitted through the spectrometer are then re-accelerated, first to their initial energy, and then by an additional 10 keV by a post-acceleration

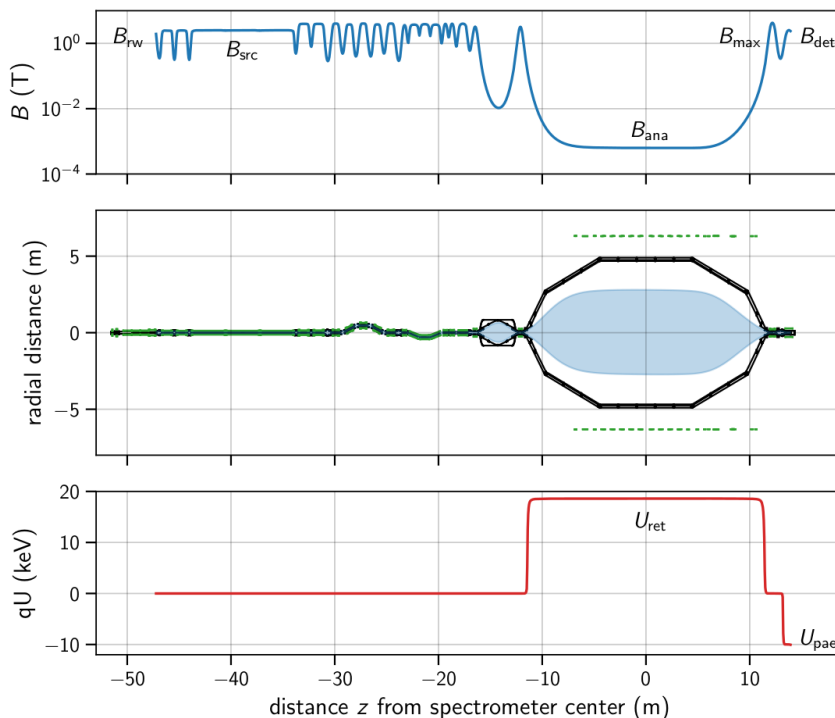


Figure 2.5: Visualization of the KATRIN electromagnetic fields. The magnetic field strength is shown on the top, the electric potential on the bottom. The center plot pictures a cross section of the beamline geometry, viewed from the top. Beam tube elements and electrodes are shown in black, magnets in green, and mapping of the flux tube to the detector in blue. Figure from [47].

electrode [46]. This reduces the backscattering probability and shifts the spectrum to a region of lower intrinsic background. The electrons are then detected by the Focal Plane Detector (FPD), a 148-pixel silicon pin diode. The pixels are arranged in 12 rings, with 12 pixels each, plus 4 pixels in the center, as can be seen in figure 2.2. This allows for the investigation of radial and azimuthal dependencies of the electron signal.

### 2.2.6 Response Function and Modelling in KATRIN

An important tool for modelling systematic effects in KATRIN is the so-called response function. In an ideal experiment, this would just be a step function showing that 0% of electrons are transmitted with initial energy lower than the main spectrometer potential, and 100% transmission is achieved for electrons with a higher initial energy. In reality, this is not the case, due to the energy resolution of the spec-

trometer, the acceptance angle, and the scattering of electrons on tritium molecules on their way out of the source. Figure 2.6 shows a measurement of the response function.

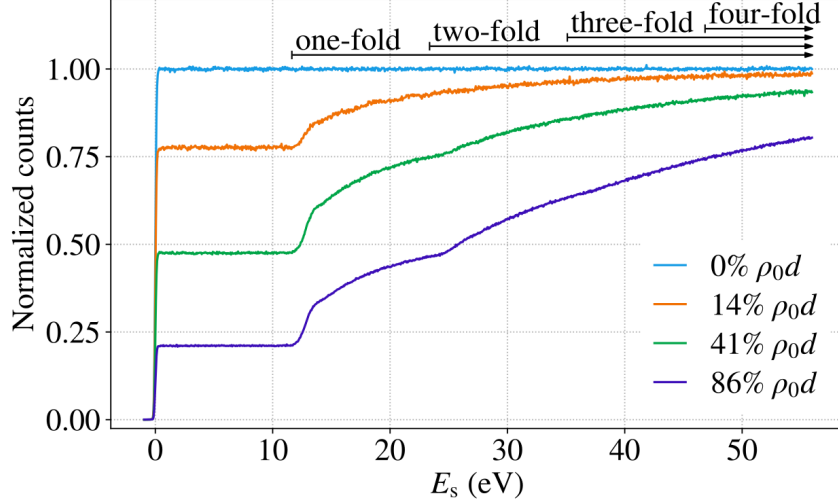


Figure 2.6: Measurement of the KATRIN response function at different fractions of the nominal column density  $\rho_0 d$ , depending on the surplus energy  $E_S$  of the electrons with respect to the spectrometer potential. It can be seen that, depending on the column density, a varying fraction of electrons does not scatter inelastically and maintains the ideal step function behaviour relatively well due to the good energy resolution of the spectrometer. Electrons that did scatter inelastically only pass if they had a higher surplus energy. Figure from [48].

The figure shows that the electrons that do not scatter inelastically (i.e. with energy loss) in the source maintain the ideal step function relatively well. However, electrons that do scatter inelastically lose at least 12.7 eV energy, corresponding to the lowest electronic excitation state of the  $T_2$  molecule. This is visible as a kink-like structure at a surplus energy of 12.7 eV. At higher source densities, a second kink can be seen at surplus energies above which electrons that scattered twice can also reach the detector.

This effect results in an optimization problem for the KATRIN experiment: The higher one sets the spectrometer potential, the less the spectrum is influenced by electrons that inelastically scattered, since they cannot have enough surplus energy to reach the detector. However, a higher minimum spectrometer potential also results in fewer counts and thus less statistics. For the latest KATRIN results, measurements were performed with an energy as low as  $E_0 - 300$  eV below the endpoint  $E_0 = 18574$  eV, but only the data for spectrometer potentials down to  $E_0 - 40$  eV

was used for the neutrino mass search [3].

A software tool to track particle trajectories and the systematic effects that influence them called KASSIOPEIA was specifically developed for KATRIN [49]. Its main purpose is to have a highly customizable, user-friendly and efficient simulation that can handle a broad variety of KATRIN-related questions. For example, KASSIOPEIA is able to compute electromagnetic fields and propagate electrons through them, while most other available programs are only optimized to do either one of the two. It also includes the possibility to simulate scattering processes in the WGTS, the principles of which served as foundation for the simulation developed in this work.

In KASSIOPEIA, electrons are propagated in small steps ("small" generally meaning on the order of the smallest feature of nearby components), with their coordinates being adjusted according to the surrounding electromagnetic fields. In a medium (such as the tritium gas in the WGTS), a distance after which the electron scatters is determined at every step and compared to the step size, to see if a scattering event happens within that step. If this is the case, the step size will be reduced to the length after which the electron scatters, and the electron's parameters are adjusted appropriately before the next step is taken. This principle of generating scattering lengths was also used for the present simulation and will be explained in the following (see sections 3.1 and 4.2.1 specifically).

However, in order to achieve an efficient simulation for scattering in the source only, it was chosen to not use KASSIOPEIA's step-by-step approach and to not simulate the electromagnetic fields at all. Instead, a more simplified and abstract model of the WGTS was chosen, which will be explained in detail in chapter 5. Before that, a general introduction to the TRISTAN project will be given after the latest KATRIN are shortly presented in the next section.

### 2.2.7 Latest KATRIN Results

The latest KATRIN neutrino mass publication contains the results of the first two physics runs (also called neutrino-mass campaigns or measurement campaigns) [3]. Main improvements of the second measurement campaign compared to the first include an operation at the nominal source activity of  $9.5 \times 10^{10}$  Bq (before:  $2.5 \times 10^{10}$  Bq) and an improvement in vacuum conditions which lead to the background being reduced by about 25% to 220 mcps. In the last 40 eV of the integral tritium spectrum,  $3.7 \times 10^6$  betaelectrons were detected. The spectral shape was obtained by measuring the count rate for 39 different spectrometer potential  $qU$  settings in the interval  $[E_0 - 300 \text{ eV}, E_0 + 135 \text{ eV}]$  around the tritium endpoint energy  $E_0$ . 28 of those points in the interval  $[E_0 - 40 \text{ eV}, E_0 + 135 \text{ eV}]$  were used to obtain a spectral fit while the remaining points at lower energy served for monitoring the activity stability. The spectral data was fitted with a spectrum prediction given by

a theoretical decay spectrum convoluted with the experimental response function and an added background rate.

For the squared effective electron antineutrino mass  $m_\beta^2 = \sum_{i=1}^3 U_{ei}^2 m_i^2$ , a best fit of  $m_\beta^2 = (0.26 \pm 0.34) \text{ eV}^2$  was obtained for the second campaign. This results in an upper limit for the neutrino mass of  $m_\beta < 0.9 \text{ eV}$  at 90% confidence level. The results from the second neutrino mass campaign were also combined with the ones from the first by performing a simultaneous fit of both data sets, giving a best fit of  $m_\beta^2 = (0.1 \pm 0.3) \text{ eV}^2$  and a corresponding limit of  $m_\beta < 0.8 \text{ eV}$  at 90% confidence level. Both results along with neutrino mass limits from previous experiments are shown in figure 2.7.

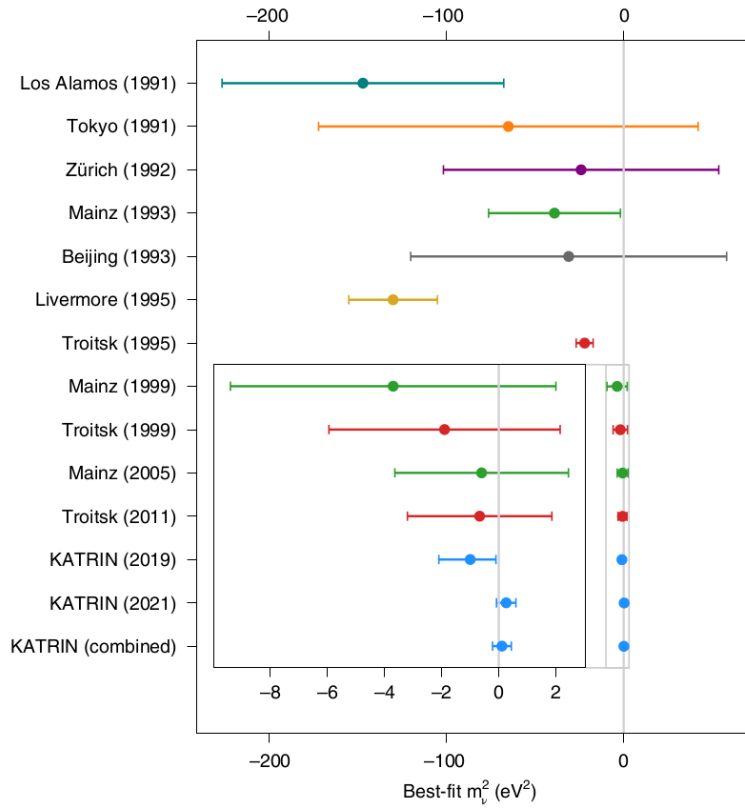


Figure 2.7: Neutrino Mass results from the first two KATRIN neutrino mass campaigns compared to results from previous experiments. Figure from [3].

## 2.3 TRISTAN - Search for keV-Scale Sterile Neutrinos

After the KATRIN neutrino mass measurements are completed, KATRIN will continue operating to search for a potential signal of sterile neutrinos on the keV mass scale, by using a new detector called TRISTAN. While it is already possible to search for sterile neutrinos on the eV-scale with the data from the current mass measurements [37], a heavier sterile neutrino would leave a trace far deeper into the spectrum. This signal has been searched for in the first KATRIN data. During a commissioning run, measurements were taken at a significantly lowered source density, allowing to probe the spectrum deeper below the endpoint and searching for a sterile neutrino of a mass up to 1.6 keV. From this search, an exclusion limit on the mixing amplitude of  $\sin^2(\theta) < 5 \times 10^{-4}$  at 95% confidence level could be set at a sterile neutrino mass of 0.3 keV, improving current laboratory limits in the 0.1 – 1 keV mass range [50]. Further improvement on this limit concerning the mass range as well as the mixing amplitude sensitivity is planned by lowering the spectrometer potential and acquiring much more statistics in a dedicated measurement. This requires significant modifications to the experimental setup.

The basic measurement idea of TRISTAN is explained in section 2.3.1. Section 2.3.2 will give an overview over the most important changes that have to be made with respect to KATRIN operation in order to search for a keV-scale sterile neutrino. Finally, section 2.3.3 will introduce the most important systematic effects limiting the sensitivity to the sterile neutrino.

### 2.3.1 Measurement Principle

The KATRIN keV sterile neutrino search measurement principle is based on the idea that, as described in section 1.4, (at least) one sterile neutrino could exist in addition to the three active neutrino flavors. This sterile neutrino would introduce an additional fourth mass eigenstate  $m_4$  and mix with the active flavors, as described by equation (1.19). If one groups the three active neutrinos into one effective "light" state  $m_\beta$  for simplicity, this results in a differential decay rate  $d\Gamma/dE$  given by:

$$\frac{d\Gamma}{dE} = \cos^2(\theta) \frac{d\Gamma}{dE}(m_\beta) + \sin^2(\theta) \frac{d\Gamma}{dE}(m_4), \quad (2.4)$$

where the size of the effect of the sterile neutrino is governed by the effective mixing angle  $\theta$  [51].

This introduces a distortion in the spectrum that is characterized by a kink-like structure located at  $E_0 - m_4$ . If the electron receives more energy than that, there is not enough energy left for the neutrinos to be produced in the heavy mass state, causing the sterile branch to end at that point in the spectrum. This causes a kink-like structure in the spectrum, which is illustrated in figure 2.8.

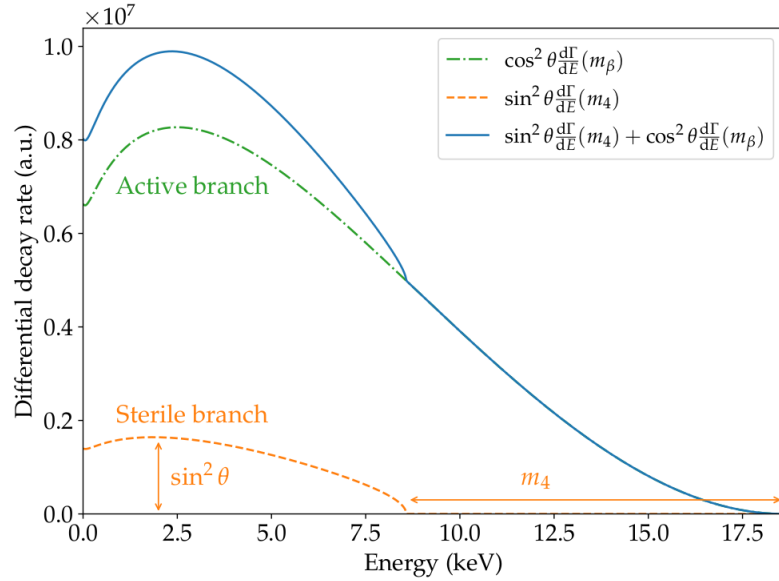


Figure 2.8: Illustration of the sterile neutrino signal in the tritium decay spectrum, for a 10 keV mass state and an exaggerated mixing angle. At an energy of 10 keV below the endpoint  $E_0$ , the heavy mass state stops being produced, resulting in a kink in the spectrum. Figure from [52].

In order to detect a signal significantly deeper into the spectrum, the spectrometer potential has to be lowered. Keeping the column density constant, this results in count rates several orders of magnitude higher than KATRIN's current rates of a few counts per second [3]. The current KATRIN detector is not designed to handle such high rates. Therefore, a new detector system is being developed, called TRISTAN, along with a lowering of the source activity. This, along with other operational changes that are made in order to reach the design sensitivity of a mixing angle of about  $\sin^2(\theta) < 10^{-6}$  [53], will be described in the next section.

### 2.3.2 Changes in Operation and New Detector System

As already mentioned, searching for a signal deep in the tritium spectrum requires significantly lowering the spectrometer voltage. A new detector system is under development that can handle the resulting high count rates. In addition, it is planned to perform a differential measurement instead of an integral measurement, meaning the energy resolution is set by the detector itself and not via filtering at the spectrometer. In order to reach a sensitivity of  $\sin^2(\theta) < 10^{-6}$ , this requires a de-

tector energy resolution of 300 eV at an electron energy of 30 keV [53]. The energy resolution of the current KATRIN FPD is about 1.5 keV at the tritium endpoint of 18.6 keV, and only marginally lower at 30 keV [54]. The detector system is designed to be able to handle count rates of up to  $\mathcal{O}(10^8)$  cps). By segmenting the detector into  $\mathcal{O}(1000)$  pixels, the electron rate reaching each individual pixel reduces to  $\mathcal{O}(10^5)$  cps) [53]. These requirements regarding resolution and count rate are met by the Silicon Drift Detector (SDD) technology, which has the additional benefit of a low energy threshold of about 2 keV [52]. The basic working principle of an SDD is shown in figure 2.9b.

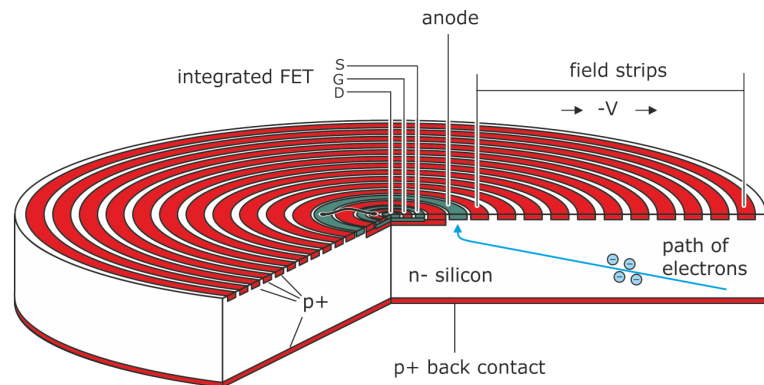
SDDs consist of an electron donor-type ("n-type") silicon substrate framed on both sides by a silicon layer doped with small fractions of other materials in order to become an electron acceptor ("p-doped"). The entrance window is made of a solid p-doped back-contact on a negative bias voltage. On the other side ("front end"), p-doped drift rings surround an n-doped anode at the center which is connected to the read-out electronics.

When a photon or charged particle enters the detector through the entrance window, valence band electrons are excited into the conduction band, creating so-called electron-hole pairs. The number of pairs depends on the energy the particle deposits in the detector and on the energy required to create a single pair, which is material-specific. The electrons then drift towards the anode, creating a measurable electrical current. Holes are collected at the back contact or the drift rings. Operating the detector at low temperature reduces noise [53].

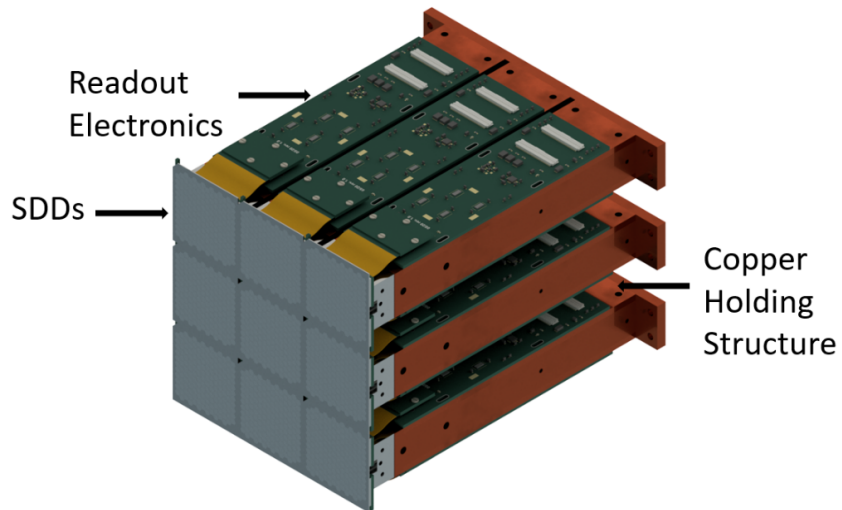
While the new detector system and the operation at low spectrometer voltages are important, other changes in KATRIN operation will also be made in order to optimize the sensitivity of TRISTAN. To name a few:

- a new DAQ system is under development that can handle the high countrates,
- magnetic fields are optimized, e.g. to reduce detector backscattering,
- the column density will be reduced by a factor of about 100 to lower count rates to a manageable level,
- a new post acceleration electrode system is under development, also to reduce detector backscattering,
- adjustments to the rear section are considered to reduce backscattering towards the detector, such as replacing the rear wall material. [47, 55].

Most of these adjustments are made in order to reduce one or more systematic effects, an overview of which will be given in the next section.



(a) Working Principle of an SDD. The p-doped back contact and the drift rings are shown in red, the anode in green. An exemplary electron drift path is also shown. Figure from [56], adapted from [57].



(b) Technical drawing of the planned arrangement of nine TRISTAN detector modules, each with 166 hexagonal pixels. This detector system is planned to replace the current FPD in the so-called *Phase 1* of the keV sterile neutrino search. In a possible *Phase 2*, a system with 21 modules will be used. Figure from [58].

Figure 2.9: Working principle of an SDD and illustration of the TRISTAN detector system

### 2.3.3 Systematic Effects and Modelling in TRISTAN

By investigating almost the entire tritium spectrum instead of just the endpoint while having access to the same high activity source as for the neutrino mass measurement, a low statistical uncertainty can be reached within a relatively short measurement time [51]. However, systematic uncertainties cannot be reduced so easily. Based on the latest investigation, using the same beamline settings as for the neutrino mass measurement, the statistical sensitivity is expected to be reduced by at least one order of magnitude [52]. A prediction of the statistical sensitivity, compared to the previous KATRIN result and other limits is shown in figure 2.10.

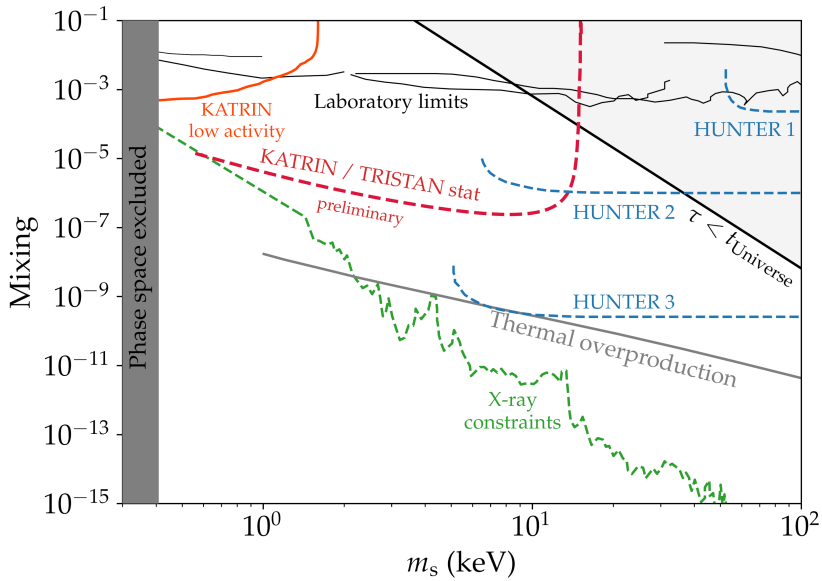


Figure 2.10: Statistical sensitivity prediction for the TRISTAN project, compared to previous laboratory and cosmological limits and the predicted sensitivity of the HUNTER project [59]. Plot adapted from [60].

Several of these systematic effects will be named here (not all of them explained in detail), going through the beamline from the rear wall to the detector:

- Rear Wall:
  - Backscattering: The current rear wall is gold-plated. Since the backscattering coefficient of electrons increases with the nuclear charge of the target material, gold has a relatively high backscattering coefficient [61]. For the neutrino mass measurement, this is not a huge issue as elec-

trons typically lose enough energy in the backscattering that they then cannot overcome the spectrometer potential. In the keV sterile neutrino search however, electrons that lose even a lot of energy can still reach the detector while carrying virtually no more information on the sterile neutrino. Therefore, modifications to the rear wall such as changing the material and optimizing the magnetic fields are being considered [47, 55].

- WGTS:
  - Electron Scattering on T<sub>2</sub> molecules: Some differences exist to the effect scattering has in the keV sterile neutrino search compared to the neutrino mass measurement. On the one hand, scattering will be significantly reduced in the keV sterile neutrino search by lowering the source density, reducing the overall impact of the effect. However, the large energy range also has an effect here: In the neutrino mass measurement, electrons only can scatter a limited number of times before they have lost too much energy to overcome the main spectrometer potential. At a lower potential, electrons can potentially scatter dozens of times, lose a significant portion of their energy and significantly change their angle and still reach the detector.
  - Magnetic Traps: The magnetic field in the WGTS has minima in the regions between magnet coils in which electrons with a high pitch angle can get trapped and only escape through scattering or non-adiabatic motion (i.e. motion that does not follow the magnetic field lines) [47, 55].
  
- Transport Section and Spectrometer:
  - Non-adiabaticity: Due to their high surplus energies, electrons can move through the main spectrometer without exactly following the magnetic field lines [56],
  - Magnetic Mirror:s Electrons can be reflected between magnetic field maxima [47].
  
- Detector and DAQ (covered in more detail elsewhere [4, 58, 62, 63]):
  - Backscattering: Electrons can deposit only part of their energy at the detector and then be backscattered from it, potentially returning to a different pixel or long enough after to be detected as a separate event.
  - Dead Layer: The entrance window of the detector has a layer of non-sensitive material where electrons can deposit part of their energy.

- Charge Sharing between pixels: A single electron can deposit its energy in two or even three adjacent pixels.
- Pile-Up: Two or more electrons hitting the same pixel within a short period of time can not be resolved as separate events.
- Crosstalk: An electron being detected in one pixel can create a signal in one or more other pixels by interaction of the read-out electronics.

In order to assess the TRISTAN sensitivity and to investigate what hardware changes are necessary, an accurate modelling of these mentioned systematic effects is crucial. For that purpose a dedicated software tool called TRModel was developed [64]. Its working principle is briefly explained below, following the description provided in the PhD thesis of Martin Descher [47] unless otherwise noted. The TRModel is based on a response matrix formalism, where a binned theoretical prediction of the tritium spectrum gets subsequently multiplied with response matrices each describing a single systematic effect. The principle of how a response matrix acts on a binned spectrum is shown in figure 2.11.

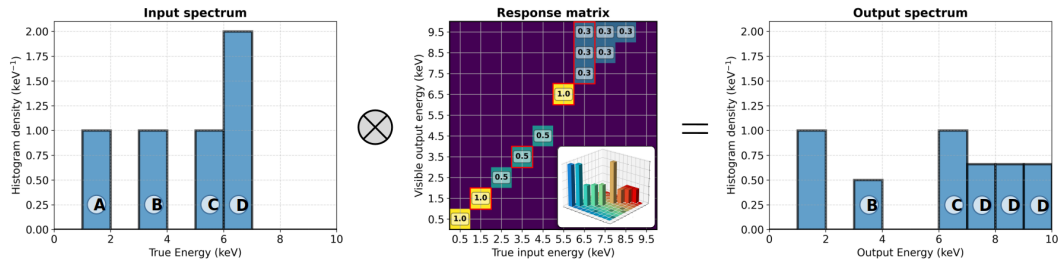


Figure 2.11: Visualization of the working principle of the response matrix formalism. A binned initial spectrum (left) gets multiplied with a response matrix (center), resulting in a final spectrum (right). Some specific effects are shown as an example: The column A appears unperturbed in the final distribution. Column B loses 50% in value, modelling e.g. a transmission efficiency. Column C is shifted one bin to the right, as would be the case when the electrons are accelerated. Finally, column D is also shifted and uniformly spread across several adjacent bins. Plot by Anthony Onillon.

The response matrices are generated using numerical calculations based on analytical descriptions or Monte Carlo simulations, depending on the respective effect. For example, effects like magnetic collimation and mirroring can be calculated analytically, while backscattering from the rear wall and the detector is modelled in a Monte Carlo simulation using the Geant4 [65] software.

There is also a model for scattering in the WGTS implemented [66]. It uses a binned convolution approach, where the WGTS is divided into a number of slices  $n$  each

containing the same fraction of the column density  $\rho d$ . The number of slices is supposed to be chosen sufficiently large so that the probability of an electron scattering more than once within one slice can be neglected. Then, a response matrix for the traversal of a slice is created based on the scattering probability and the scattering cross sections (see chapter 3). The matrix is iteratively applied  $n$  times to the initial spectrum, once for the traversal of each slice. This approach was chosen to avoid the statistical fluctuations of a Monte Carlo simulation and due to its efficiency. The calculation is performed using Graphics Processing Unit (GPU) computation in which matrix multiplication is a highly optimized process. However, there are also some issues: this software is not very well documented and none of the developers is currently actively involved in TRISTAN. On top of that, the program shows issues when going to a very fine binning, and there is currently no way to evaluate the accuracy of it.

Therefore, it was chosen to develop an additional Monte Carlo simulation for scattering in the WGTS, which is the purpose of this work. In the following, first some background will be provided on scattering physics and random number generation in the chapters 3 and 4, before the working principle of the simulation will be explained in chapter 5.

## Chapter 3

# Electron Scattering on Gas Atoms and Molecules

In order to simulate scattering in the WGTS, the underlying physical processes have to be well understood. In the energy range of the tritium decay, scattering processes are typically described by solving the non-relativistic Schrödinger equation. Any structural relativistic effects are thereby neglected, but relativistic kinematics can be accounted for depending on the specific approach used for the different scattering processes.

Literature on scattering involving tritium molecules is extremely sparse. Therefore, the results presented below are based on regular hydrogen, with corrections applied for the higher mass of tritium wherever possible. Other than that, corrections are assumed to be small, since all the electric charges stay the same. This is confirmed to a degree by experimental data that is available for deuterium which shows only very small deviations to the regular hydrogen molecule, such as the measurement by Ketkar and Fink of 40 keV electrons crossing a ( $\text{H}_2$  or  $\text{D}_2$ ) molecular gas jet [67]. The parameter one typically wants to extract from a scattering calculation is the cross section  $\sigma$ . It has units of  $\text{m}^2$  and in the classical analogy represents an effective surface the target material has "from the point of view" of the projectile. In its (double) differential form  $d\sigma/dE$  ( $d^2\sigma/dEd\Omega$ ) it provides additional information on the probability of specific changes in parameters.

A short introduction on the most important aspects of scattering physics as well as the Bethe theory, which is the basis for most scattering calculations for electrons in the low keV energy region, will be given in section 3.1. In the following sections, an overview will be given on the cross sections used to describe the different scattering processes implemented in the simulation: first on the total cross sections (section 3.2), then on elastic scattering (section 3.3), electronic excitation of the tritium molecule (section 3.4) and eventually on ionization (section 3.5).

### 3.1 Introduction and Bethe Theory

Due to the nature of quantum mechanics, scattering of particles is an intrinsically stochastic process. Assuming the scattering probability stays constant, the probability  $P$  of a particle moving through a medium having scattered at least once after travelling a distance  $x$  asymptotically approaches 1 [68]:

$$P(x) = 1 - \exp\left(-\frac{x}{\lambda}\right). \quad (3.1)$$

The parameter  $\lambda$ [m] is called the mean free path and depends on the target particle density  $\rho$ [ $\frac{1}{\text{m}^3}$ ] and the total scattering cross section  $\sigma$ :

$$\lambda = \frac{1}{\rho \cdot \sigma}. \quad (3.2)$$

This means determining the scattering probability requires a determination of the density  $\rho$  as well as the cross sections  $\sigma$

The total cross section  $\sigma$  is a theoretical representation of the overall probability that a scattering process will happen between two types of particles. The (double) differential cross section  $d\sigma/dE$  ( $d^2\sigma/dEd\Omega$ ) contains additional information on the probability of a certain output energy and scattering angle.

Scattering at the particle level heavily depends on the kinetic energy in the system of the two interacting particles, viewed from the rest frame of the center of mass. In a lot of cases, such as the present one of electrons scattering on molecules, one of the considered particles is much heavier than the other, and one typically names the lighter, fast particle the "projectile" and the heavier, (almost) at rest particle the "target". Determined by its momentum  $\mathbf{p}$ , the projectile can be associated with a certain wavelength, given by the de-Broglie relation [13]:

$$\lambda_{\text{dB}} = \frac{1}{|\mathbf{p}|}. \quad (3.3)$$

This wavelength determines on which length scales the projectile interacts, i.e. what the particle "sees". In the low keV energy range of the tritium beta electrons,  $\lambda_{\text{dB}}$  is of order  $\mathcal{O}(10^{-11} - 10^{-10} \text{ m})$ . This is the same order of magnitude as the Bohr radius (i.e. the effective radius of the hydrogen atom)  $a_0 = 5.29 \times 10^{-11} \text{ m}$ , meaning that the electrons from the tritium decay will mainly interact with the tritium atoms, as opposed to e.g. the entire molecule or the nucleus. However, it is still relevant that the tritium is bound in molecules, since this changes the energy levels as well as the ionization energy.

Most scattering calculations in this energy region to this day are based on the Bethe theory, which was published in 1930 [69]. A short overview of its principles will be

given here, mainly using a more modern notation taken from [70].

The Bethe theory employs the Born approximation, in which the interaction terms of the Schrödinger equation are developed in a series of rising powers of  $(R/E)$  with  $R = 13.6 \text{ eV}$  the ionization energy of the hydrogen ("Rydberg energy") and  $E$  the kinetic energy of the projectile. This series then gets cut after the first term. Since the next term in the series is suppressed by a factor of  $R/E$ , this approximation is valid to the percent level for energies down to about 1 keV.

Using this approximation, one can derive a formula for the differential cross section of a scattering process that changes the initial state of the system 0 to a final state  $n$ :

$$\frac{d\sigma_{0,n}}{d\Omega}(\mathbf{K}) = \frac{M^2}{2\pi} |\mathcal{V}_{0,n,\mathbf{K}}|^2 \frac{k_f}{k_i}, \quad (3.4)$$

with  $M = \frac{M_{\text{projectile}} M_{\text{target}}}{M_{\text{projectile}} + M_{\text{target}}} \approx M_{\text{projectile}}$  being the reduced mass of the system,  $k_i = |\mathbf{k}_i|$  and  $k_f = |\mathbf{k}_f|$  the magnitudes of the initial and final projectile momenta and  $\mathbf{K} = \mathbf{k}_f - \mathbf{k}_i$  the momentum transferred. The transition matrix element

$$\mathcal{V}_{0,n,\mathbf{K}} = \int d\tau d\mathbf{r} e^{i\mathbf{K}\mathbf{r}} \psi_0 V(t) \bar{\psi}_n$$

between the initial state  $\psi_0$  and the final state  $\psi_n$  of the system contains the potential  $V(t)$ . It describes the coulombic interaction between the projectile and the nucleus as well as between the projectile and the target electrons. The matrix element is obtained by integration over the nucleus coordinate  $\mathbf{r}$  as well the set of electron locations  $d\tau = dr_1 \dots dr_Z$ . It is noteworthy that while the notation implies a discrete final state  $n$ , the same calculation applies also for continuous final states (i.e. ionization) if one takes the differential  $d/dE$  on both sides of eq. (3.4) [70].

Through clever choice of integration order, Bethe then calculated a differential cross section formula of

$$\frac{d\sigma_{0,n}}{d\Omega}(\mathbf{K}) = 4z^2 M^2 |\epsilon_{0,n}(\mathbf{K})|^2 \frac{k_f}{k_i} \frac{1}{K^4}, \quad (3.5)$$

with the projectile charge  $z$  and the so-called atomic matrix element

$$\epsilon_{0,n}(\mathbf{K}) = \langle \psi_n | \sum_{j=1}^Z \exp(i\mathbf{K}\mathbf{r}_j) | \psi_0 \rangle,$$

which sums over the number of target electrons  $Z$ . The calculation of these matrix elements is the main challenge of solving a scattering problem. This is not trivial even for a very simple molecule like hydrogen. Thus, there is only a limited amount of literature on this subject in the energy region of interest. The same is true for experimental data, making it difficult to evaluate the uncertainties associated with the cross sections. Nevertheless, an attempt has been made to at least provide a

rough estimate of the uncertainties of the given cross section formulas.

The following sections will cover the cross sections used in the simulation, as well as a short explanation on the process they describe and how they are obtained.

### 3.2 Total Cross Sections

As mentioned above, total cross sections directly relate to the scattering probability via the mean free path, as described in equations (3.1) and (3.2). In principle, they can be obtained by integrating the differential cross sections of the individual processes described in the sections below. However, since the differential cross sections available in literature for the different processes are usually calculated using different approaches and partly more focused on the correct output parameter distribution than the overall normalization, it was chosen to rather take a single source for the values of the total cross sections.

Formulas for the total elastic as well as inelastic cross sections for electron scattering on hydrogen molecules as a function of the electron energy have been determined by J. W. Liu [71].

Using a revised version of the Bethe theory, Liu gives a total elastic cross section of

$$\sigma_{\text{el}}(T) = \pi a_0^2 \cdot \frac{R}{T} \cdot \left( 4.2106 - 2 \frac{R}{T} \right), \quad (3.6)$$

where  $R$  is the Rydberg energy and  $T = \frac{mv^2}{2}$  the non-relativistic kinetic energy of the electron. In order to correct for kinematic relativistic effects, the electron energy  $E$  from the decay is converted to the non-relativistic kinetic energy  $T$  by calculating the velocity:

$$v^2 = 1 - \frac{m_e^2}{(m_e + E)^2}. \quad (3.7)$$

At an electron energy of 25 keV (corresponding to a non-relativistic kinetic energy of 23.3 keV using eq. (3.7)), the elastic cross section formula (3.6) evaluates to  $0.00773a_0^2$ . Liu compares this to an experimental value of  $(0.00789 \pm 0.00010)a_0^2$  found by Ulsh et al. [72]. The two values are in good agreement with a difference of  $2.1 \pm 1.3\%$ .

The total inelastic cross section is given as

$$\sigma_{\text{inel}}(T) = 4\pi a_0^2 \frac{R}{T} \left( 1.5487 \cdot \ln \left( \frac{R}{T} \right) + 2.4036 + \gamma_{\text{tot}} \frac{R}{T} \right), \quad (3.8)$$

with

$$\gamma_{\text{tot}} = 2Z \left( -\frac{7}{4} + \ln \left( \frac{E_{\text{ion}}}{T} \right) \right),$$

$Z = 1$  the target atom electron number and  $E_{\text{ion}} = 15.43$  eV [73] the electron binding energy of the target (here, the hydrogen molecule).

The calculation of the numerical values in the cross section mostly involves solving integrals and evaluating special functions and will not be discussed in detail here.

The value of  $\sigma_{\text{el}} + \sigma_{\text{inel}}$  is used to determine if a scattering happens (i.e. the scattering probability, see chapter 5 for details). To then decide which process occurs, the elastic cross section is used again together with functions for the total ionization and excitation cross section from another publication by Liu [74]. There, the formula for the inelastic cross section is fitted to experimental data for ionization, excitation as well as dissociation of the molecule. The resulting functions are then used to determine if an ionization or excitation process happens. The smaller effect of dissociation is not included as a separate process, it is assumed that the molecule dissociation happens after an excitation to a high energy state and thus the dissociation cross section is added to the excitation cross section. This assumption needs further evaluation in the future though, as dissociation after ionization can in principle also happen. Liu also combines experimental values from several sources on the different scattering types to a single inelastic cross section formula given by

$$\sigma_{\text{inel,exp}}(T) = \frac{4\pi a_0^2 R}{T} \left( M_{\text{tot}}^2 \ln \left( \frac{T}{R} + A \right) \right), \quad (3.9)$$

where  $M_{\text{tot}}^2 = (1.51 \pm 0.13)$  and  $A = (1.58 \pm 0.46)$  are determined using experimental data [74]. Figure 3.1 shows a plot of the total cross section functions resolved by scattering type as well as a comparison of the theoretical inelastic cross section function (eq. (3.8)) to the empirical one (eq. (3.9)).

In plot 3.1a, it can be seen that the ionization and excitation cross sections are on the same order of magnitude, while elastic scattering is a significantly smaller effect. Overall, scattering becomes more probable the lower the energy of the electron is. Comparing the theoretical and empirical cross section (plot 3.1b), one can see that the two results deviate by about 10%, but agree within the uncertainty of the fit parameters.

Considering the comparison to experimental data for the inelastic and elastic cross sections as well as the approximations that are made in the theoretical calculations (Born approximation, non-relativistic approximation, numerical evaluation of integrals), the overall uncertainty of the total cross sections can be roughly estimated to lie on the level of a few percent.

### 3.3 Elastic Scattering

Differential cross sections contain information on the probability of certain output parameters of a scattering process. This generally means the energy of the electron

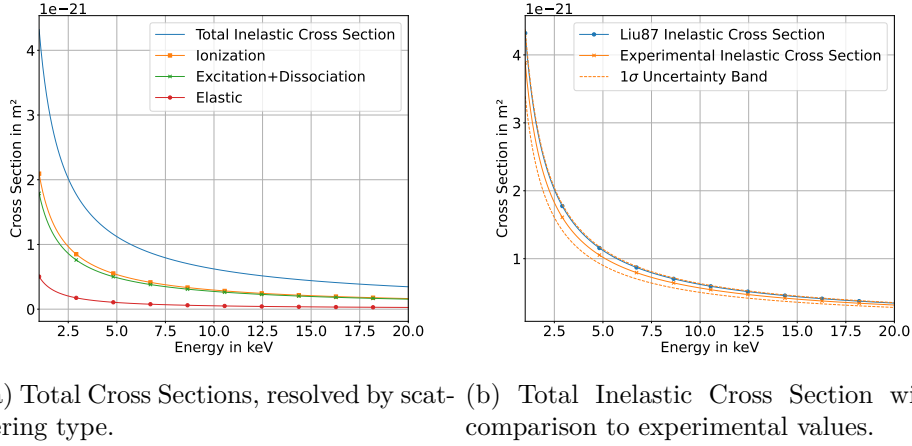


Figure 3.1: Plot of the total cross sections in the energy region of the tritium beta electrons (a). Ionization and Excitation scattering are dominant, while elastic scattering is a smaller effect. The cross section increases for lower electron energies. Also shown is a comparison of the total inelastic cross section to a fit to experimental data taken from [74] (b). There is a difference of about 10% which lies within the uncertainty of the experimental fit parameters.

and its angle with respect to its previous direction.

Although technically not quite correct, one typically summarizes all scattering processes where the electron loses a negligible amount of energy under the name *elastic scattering*. This includes the "true" elastic scattering process where the molecule is left in the same energetic state as before the scattering, but also processes where the molecule is excited to a purely rovibrational energy level. Both result in a negligible energy loss on the order of meV and are therefore often considered together, sometimes also under the term *quasielastic*. For the purposes of the simulation developed here, this small energy loss is neglected and the differential cross section then only depends on the angle change of the electron.

A differential elastic cross section has been calculated by Kołos et. al. [75]. It consists of a contribution  $N_{\text{IAM}}$  of the so-called independent atom model along with corrections  $\Delta N_{\text{qel}}$  that are provided as tabulated values in the paper:

$$\frac{d\sigma_{\text{el}}}{d\Omega}(K) = \frac{4a_0^2}{K^4} (N_{\text{IAM}} + \Delta N_{\text{qel}}). \quad (3.10)$$

It is given as a function of the momentum transfer  $K$ , which directly depends on the scattering angle  $\theta$  and the electron energy  $E$ :

$$K = 2\sqrt{\frac{E}{2R}(1 - \cos(\theta))}. \quad (3.11)$$

The independent atom model contribution is given by:

$$N_{\text{IAM}} = 2 \cdot \left(1 - \frac{1}{(1 + K^2/4)^2}\right)^2 \cdot \left(1 + \frac{\sin(KD)}{KD}\right), \quad (3.12)$$

with the average distance  $D = 1.4009$  of the atoms in the molecule, given in units of  $a_0$ . It comes from considering two individual hydrogen atoms separated by a distance  $D$  and allowing for a phase difference of the scattered waves emanating from the two atoms, resulting in the sine contribution [76].

Unfortunately, this cross section formula diverges for very small  $K$ , i.e. small scattering angles  $\theta$ . Therefore, in the region of  $K < 1$ , a different approach is chosen, given by Komasa and Thakkar [77]. It is an expansion in  $K^2$  and therefore only valid for  $K < 1$ :

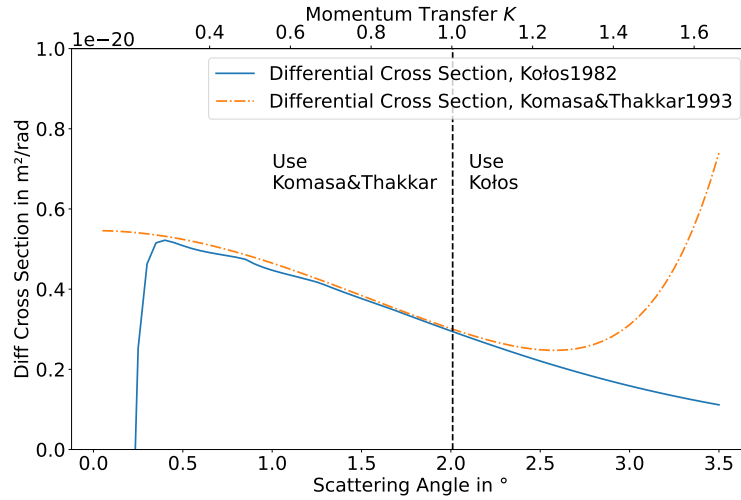
$$\frac{d\sigma_{\text{el}}}{d\Omega}(K) = \gamma^2 a_0^2 \sum_{i=0}^{\infty} A_{2i} K^{2i}, \quad (3.13)$$

with the relativistic Lorentz factor  $\gamma$  and tabulated coefficients  $A_{2i}$  for an expansion up to  $K^8$ .

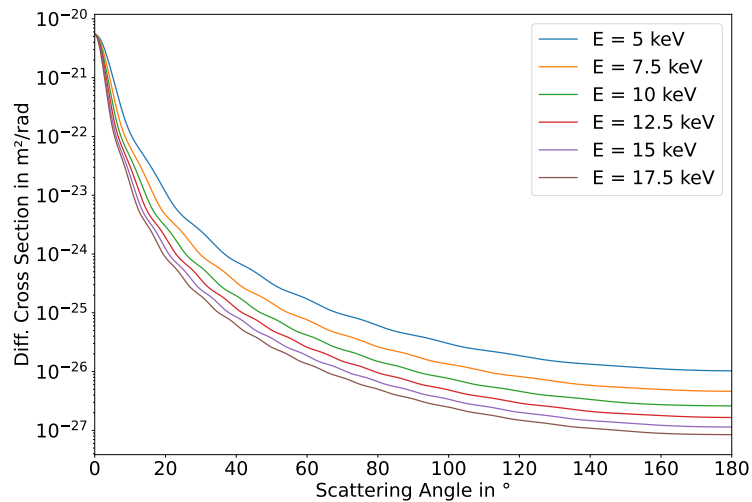
It was chosen to use this cross section for  $K < 1$  and the Kolos cross section for larger  $K$ . Figure 3.2 shows the behaviour of both cross sections for low  $K$  values as well as the combined cross section used in the simulation.

The cross section rapidly decreases for larger scattering angles, making scattering at a low angle far more probable. Also, for increasing electron energies, the cross sections get smaller, as expected from the total cross section shown in figure 3.1. One can also see an oscillation in the angle distribution. This comes from the sine contribution in the independent atom model, given by eq. (3.12).

Kolos et. al. compare their results for the deviation from the independent atom model  $\Delta N$  for their total cross section to experimental data obtained by Ketkar and Fink [67]. The values agree within a few percent for low  $K$  values, but deviate up to a few 10% for  $K > 3$ . However, in that region the contribution of the  $\Delta N$  correction terms to the total cross section also lies below 10%. Assuming a similar situation for the elastic cross section, the overall uncertainty can again be estimated to lie within a few percent. Kolos et. al. also explicitly mention that they do not believe a further significant numerical improvement of their results to be possible without touching some basic theoretical assumptions. Namely they state the Born approximation, the Born-Oppenheimer approximation (i.e. separating the electron



(a) Comparison of the behaviour of the elastic differential cross sections from Kołos et al. and Komasa and Thakkar for a small momentum transfer  $K$  and an electron energy of 10 keV. The former starts to diverge for small values of  $K$ , the latter for  $K > 1$ .



(b) Differential elastic cross section for different electron energies. It can be seen that the cross section decreases steeply for increasing angles, meaning that small angle scattering is much more probable. Also, the overall cross section values become lower for higher electron energies, which is consistent with the total cross section shown in figure 3.1.

Figure 3.2: Result for the differential elastic cross section. The cross section from Kołos et al. [75] is used for most of the angle range, but is replaced by the expansion from Komasa and Thakkar [77] for momentum transfer  $K < 1$ , corresponding to small angles.

and nucleus wave functions) and the closure procedure in the summation over the molecule final states as possible reasons for the remaining deviation, assuming the third option to be the most likely one.

Komasa and Thakkar find an agreement within uncertainties of their expansion coefficients with experimental data taken for 30 keV electrons by Zhang et al. [78]. It is also worth mentioning that Komasa and Thakkar made their calculation for D<sub>2</sub> as well as H<sub>2</sub> molecules. The resulting coefficients show a deviation of < 1% for the dominating terms, further confirming the assumption that the isotopic difference is only a minor effect.

### 3.4 Electronic Excitation

While in an elastic scattering process only the angle of the electron changes, inelastic scattering is more complicated in the sense that the electron also loses energy, adding the output energy as an additional parameter to the cross section. In the case of (electronic) excitation, the energy loss of the electron corresponds to the energy required to lift a bound electron from the molecule onto a higher energy level.

The differential cross section for excitation to the excited state  $E_n$  (corresponding to an electron energy loss of  $\Delta E = E_n$ ) is given by [79]:

$$\left(\frac{d\sigma}{d\Omega}\right)_n = 2a_0^2 R \frac{k_f}{k_i} \frac{\mathcal{R}_{\text{ex}}}{E_n K^2} f_n(K) \quad (3.14)$$

with the exchange correction

$$\mathcal{R}_{\text{ex}} = 1 - \frac{K^2}{k_f^2} + \frac{K^4}{k_f^4}.$$

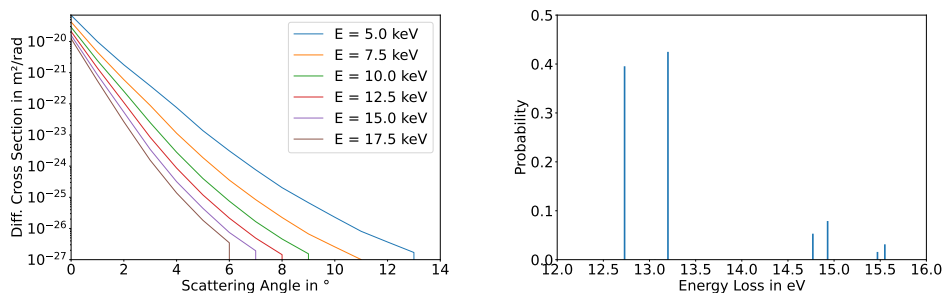
The *generalized oscillator strength*

$$f_n(K) = \frac{E_n}{R(Ka_0)^2} |\epsilon_{0,n}(\mathbf{K})|^2$$

contains the atomic matrix element from equation (3.5) [70]. Note that due to the electron losing an energy of  $\Delta E$ , the momentum transfer  $K$  is defined slightly differently [79]:

$$K = 2 \sqrt{\frac{E}{2R} \left( 1 - 2 \frac{\Delta E}{R} - \sqrt{1 - \frac{\Delta E}{E}} \cos(\theta) \right)}. \quad (3.15)$$

This is consistent with the previous definition since setting  $\Delta E = 0$  retrieves eq. (3.11).



(a) Angle distribution, for different electron energies (b) Electron energy loss, for 10 keV electrons.

Figure 3.3: Result for the excitation scattering, using the results from Arrighini et al. [80]. For the angle distribution, a linear interpolation has been performed between the tabulated values. The energy loss corresponds to the 7 excitation states considered in the calculation by Arrighini et al., one of which (at 13.1 eV) is too small to be easily seen in the plot.

Results for  $f_n(K)$  have been calculated by Arrighini et. al [80] for the dominant energy states and 15 values of  $K$  between 0 and 5. An angle distribution for the simulation is obtained by a linear interpolation between those values. The energy loss is averaged over the finer splitting of the states through rotational excitation of the molecule.

Figure 3.3 shows the angle dependence of the cross section for different energies as well as the energy loss distribution for 10 keV electrons. One can see a cut-off in the angle distribution at the point where no more tabulated coefficients are provided ( $K > 5$ ). Concerning the accuracy of these results, Arrighini et al. do not provide a detailed comparison to other data. A comparison at low incident energies  $< 100$  eV shows a deviation to other results of about 15%, but this is neither the region of interest for this work nor the region where the Born approximation is valid. An additional uncertainty to the results of the paper is introduced by doing a linear approximation between values that span several orders of magnitude, as shown in plot 3.3a.

Therefore, improvement on the excitation description is planned for the future by integrating results based on calculations specifically performed for KATRIN [70].

### 3.5 Ionization

In an ionization scattering process, an electron from the molecule is freed by the impact of the *primary* beta electron. While improbable, this so-called *secondary*

*electron* can receive so much energy in the scattering that it can be detected in the low energy region of the spectrum. This adds an additional level of complexity to this process, because not only the energy and angle distribution of the primary electron ( $E_1, \theta_1$ ) have to be known, but also those of the secondary ( $E_2, \theta_2$ ). For the energy, this is straightforward:

$$E_2 = E - E_1 - E_{\text{ion}}, \quad (3.16)$$

with  $E$  the energy of the primary electron before the scattering and  $E_{\text{ion}} = 15.43 \text{ eV}$  the electron binding energy.

However, determining the angle of the secondary, this is not as straightforward, since most publications on ionization do not provide any information on it. Therefore, an approximation is made: the exact parameters of the secondary electron are only of interest if it receives a significant amount of energy, since only then it can be detected. This amount of energy is limited by the spectrometer potential. In that case, the momentum transfer to the molecule is very small, and conservation of momentum between the two electrons is approximately given [69]. The secondary electron angle can then simply be calculated knowing all the other kinetic parameters.

This approach might eventually be improved upon through a secondary angle distribution for hydrogen atoms calculated by Mott and Massey [81]. First investigations on this distribution show that the approximation currently implemented is good (deviation  $< 1\%$ ) for a secondary electron energy of more than 1 keV [82].

While the secondary electrons are relevant, one is mostly interested in the change of the primary electron parameters. In the simulation, this information comes from a double differential cross section calculated by M. E. Rudd [83], which is also used in the existing TRISTAN source simulation [66] as well as KASSIOPEIA [49].

Rudd does not distinguish between the primary or secondary electron, resulting in a symmetric energy distribution over the whole range, while in the simulation, as in several other works, the electron with the higher energy is defined to be the primary one. An empirical approach is employed to give an analytical formula for the double differential cross section, depending on the initial electron energy  $E$ , the outgoing energy  $E'$  and the scattering angle  $\theta$  [83]:

$$\frac{d^2\sigma}{d\theta dE'}(E, E', \theta) = G_1 \left( \frac{1}{1 + [(\cos(\theta) - G_2)/G_3]^2} + \frac{G_4}{1 + [(\cos(\theta) + 1)/G_5]^2} \right), \quad (3.17)$$

with

$$\begin{aligned}
 G_1 &= 8\pi a_0^2 \frac{R^2}{E_{\text{ion}}^2} \frac{F f_1}{E_{\text{ion}}(g_{BE} + g_b G_4)}, \\
 G_2 &= \sqrt{\frac{E' + E_{\text{ion}}}{E}}, \\
 G_3 &= \beta \sqrt{\frac{1 - G_2^2}{E'/E_{\text{ion}}}}, \\
 G_4 &= \gamma \frac{E_{\text{ion}}(1 - E'/E)^3}{E(E'/E_{\text{ion}} + 1)}, \\
 F &= \frac{E_{\text{ion}}}{E} \left( A_1 \ln(E/E_{\text{ion}}) + A_2 + A_3 \frac{E_{\text{ion}}}{E} \right), \\
 f_1 &= \frac{1}{(E'/E_{\text{ion}} + 1)^n} + \frac{1}{((E - E')/E_{\text{ion}})^n} - \frac{1}{[(E'/E_{\text{ion}} + 1)((E - E')/E_{\text{ion}})]^{\frac{n}{2}}}
 \end{aligned}$$

and

$$g_{BE} = 2\pi G_3 \left[ \arctan\left(\frac{1 - G_2}{G_3}\right) + \arctan\left(\frac{1 + G_2}{G_3}\right) \right].$$

$R$  and  $a_0$  are again the Rydberg energy and the Bohr radius, the parameters  $A_1$ ,  $A_2$ ,  $A_3$ ,  $n$ ,  $G_5$ ,  $\beta$ ,  $\gamma$  and  $g_b$  are provided as numerical values, obtained by fits to experimental data from various sources [84–88].

A 2D plot showing the cross section dependency on  $E'$  and  $\theta$ , as well as an integration over either one of the parameters is shown in figure 3.4.

Rudd points out that there is some disagreement of the available experimental values with each other, making it difficult to gauge the accuracy of this model. Measurements performed to determine the energy loss in KATRIN have been compared to the Rudd cross section before [89]. It was found that other methods, such as the Binary Encounter Dipole (BED) model [90] (which was developed among others by Rudd a few years after the result used here), match the experimental data better. However, the BED model only provides an energy loss distribution and no information on the angle. Therefore, it was chosen, for the time being, to use the Rudd cross section for the simulation. Eventually, this might be improved either by combining different models or by performing own calculations, as for the excitation. While the physics knowledge on the cross sections is crucial, for a Monte Carlo simulation, additional techniques are needed to generate samples from them, which will be covered in the next chapter.

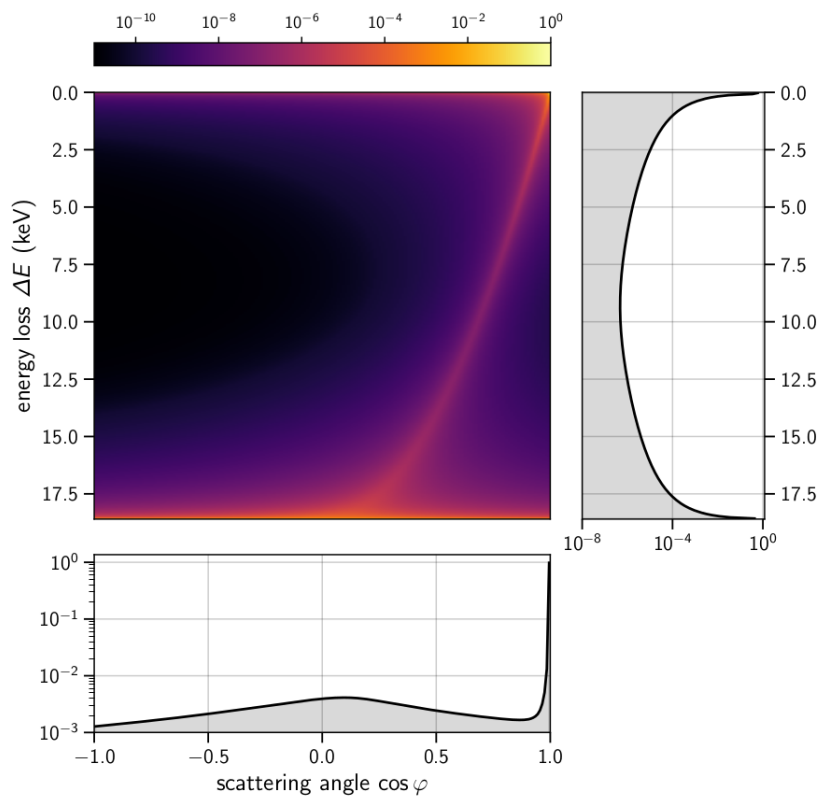


Figure 3.4: 2D Plot of the Rudd double differential ionization cross section, for electrons of initial energy 18.575 keV. An integration over the angles is shown on the right, an integration over the energy loss on the bottom. Since Rudd does not distinguish between primary and secondary electron, the former is symmetric. For each energy loss value, there is a certain angle with increased probability, called binary encounter peak or Bethe ridge [83]. Plot by M. Descher [47], using the TRISTAN source simulation [66].



## Chapter 4

# Monte Carlo Simulations, Markov Chains and Random Number Generation

Monte Carlo simulations are an important tool in many areas of research, made possible by the development of computers powerful enough to execute them. In general, they are used in many cases where either the processes described are too complicated for a more classical approach, or where an inherently random process is to be simulated [91]. The latter is the case here with scattering of electrons in the tritium source gas, as described in the previous chapter. Monte Carlo simulations require the generation of random numbers, potentially involving drawing samples from complicated distributions. In the case of the source simulation, sampling from the differential cross sections is needed to determine the output parameters of a scattering process.

The basic principles of the Monte Carlo method and random number generation will be introduced in the first section of this chapter, 4.1. Unless otherwise noted, information presented in that section comes from [91]. Section 4.2 will then explain some common methods to draw random numbers from non-trivial distributions, with an emphasis on Markov Chains, which are employed to draw samples from the differential cross sections. A small performance comparison of the different methods is also provided in this section.

### 4.1 Monte Carlo Principle and Random Numbers

In its most general definition, any method that employs random numbers to solve a problem is called a Monte Carlo method. This is possible if the problem at hand can be reduced either to the need of sampling from a distribution or to estimate the expectation value from that distribution [92].

While Monte Carlo methods can be applied to many deterministic or analytical problems, such as solving integrals, they are particularly well-suited for problems that inherently involve randomness. This is the case for electrons scattering in the KATRIN WGTS. How long an electron moves through the tritium gas before it scatters is random as well as how much its energy and angle change during a

scattering event. The expected outcome, i.e. the probability distribution is described by the scattering cross sections.

When speaking of distributions in this context, one generally means the probability density function (PDF), here called  $g(x)$ , of a continuous variable  $x$ . When a sample  $x'$  is generated, it gives the probability that  $x'$  is within an infinitesimal distance  $dx$  of the given value  $x$ :

$$g(x)dx = P(x < x' < x + dx). \quad (4.1)$$

Its integral is called the cumulative distribution function (CDF) and gives the probability that  $x'$  is smaller than or equal to  $x$ :

$$G(x) = \int_{-\infty}^x g(u)du. \quad (4.2)$$

An example for a PDF and corresponding CDF is shown in figure 4.1 along with a visualization of the inverse transform sampling method which is covered in section 4.2.1.

The kind of simulation that was developed in the context of this thesis and that is generally very commonly used in particle physics is called an event-by-event simulation. In the present case, this means that an individual electron is created with random parameters and its way through the source is simulated, including all the scattering processes that happen, until it leaves the source. Then, a second electron is generated, and so on until one has a statistical understanding of their general behaviour. In the case of the WGTS simulation, the goal is to simulate at least 10-100 times as many electrons as are measured in the actual experiment, in order to have a lower statistical uncertainty in the simulation than in the experimental data. This could mean simulating up to  $10^{17}$  electrons (with  $10^{15}$  events being expected for 1 year of data taking) [51], which is at least on the very limit of what is computationally feasible. Therefore, sampling random numbers in an efficient way is crucial, which is why the Markov Chain approach was chosen.

Before going into detail on the sampling from distributions, it should be mentioned that creating random numbers in general is a challenge on a computer, since there (normally) are not any inherently random processes measured. Therefore, one relies on so-called pseudo-random numbers generated by an algorithm. These appear random in the sense of following a given (usually uniform) distribution while actually being deterministic [93]. For the simulation developed in this thesis, the Mersenne twister algorithm [94] is employed to generate uniformly distributed random numbers between 0 and 1, as well as binary decisions (0 or 1). These are then used to generate samples from the desired distributions using either the inverse transform method or Markov Chains, both of which will be explained in the next section.

## 4.2 Sampling from a Distribution

As mentioned before, to determine the new parameters in a scattering process, samples from the differential cross sections are needed. These are, for the purposes of the simulation, known analytical functions (see chapter 3). However, knowing a distribution is generally not sufficient to draw samples from it. Some methods that can be used to draw samples from non-trivial distributions and their advantages and disadvantages will be explained in this section. Section 4.2.1 will cover the inverse transform method, section 4.2.2 will discuss the acceptance-rejection algorithm and section 4.2.3 will provide a little more detail about Markov Chains and how they can be used to generate samples.

### 4.2.1 Inverse Transform Method

The working principle of the inverse transform method is simple: one samples numbers uniformly and transforms them in a way that they match the desired distribution (i.e. PDF) [95]. This is done by inverting the CDF and drawing samples between 0 and 1 from the "probability space". A graphical illustration on this principle is shown in figure 4.1.

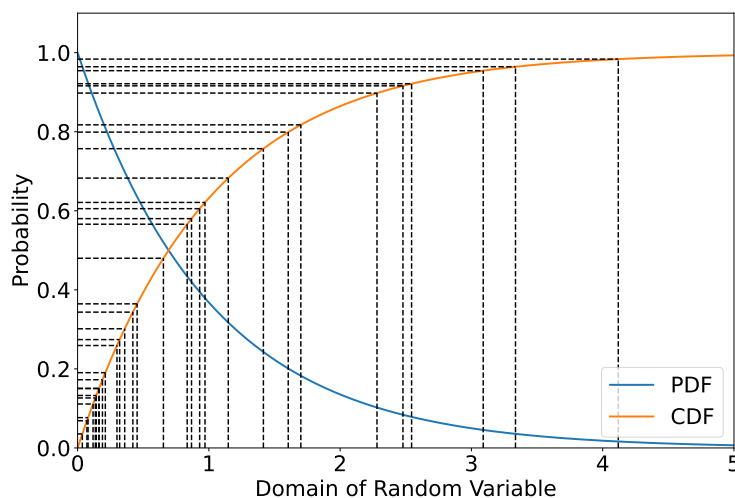


Figure 4.1: Visualization of the inverse transform sampling method. Giving uniformly distributed samples between 0 and 1 (represented as horizontal lines, i.e. y-values) to the inverted CDF returns samples distributed according to the PDF as an output (represented as vertical lines, i.e. x-values).

The CDF is the steepest where the PDF takes its highest value, i.e. where the probability to get a sample is the highest. The steeper the CDF, the more "space" it covers in the  $y$  direction, which is where the samples are drawn from. Thus areas with a high PDF are more likely to be sampled, just as desired.

This method has several advantages: it is very efficient, since generating a sample only requires drawing one uniform number along with a single function evaluation of the inverted CDF. This can be done on demand, whenever a sample is needed, and no additional bias on the numbers is introduced on top of whatever bias the uniform sample might have.

However, restrictions arise from the requirements to use this method: one needs to know the inverted CDF. Analytically, this is only possible in simple cases. While numerical inversion is possible, it either needs to be explicitly done every time a sample is generated, or it has to be performed for a set of points in advance along with a fit or interpolation. This is computationally more expensive and introduces additional uncertainties. Interpolation is also not easily possible in multiple dimensions, such as for the ionization cross section (see section 3.5).

Therefore, the inverse transform method is not used to sample from the cross sections. However, the CDF describing the probability for an electron to have scattered after travelling a certain distance (given by equation (3.1)) can easily be inverted to

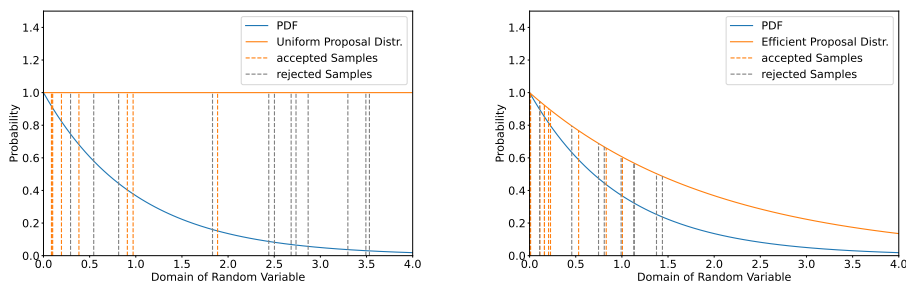
$$x = -\lambda \ln(1 - P). \quad (4.3)$$

Here, the inverse transform method is used to generate lengths  $x$  the electrons travel before they scatter by sampling  $P$  uniformly between 0 and 1.

### 4.2.2 Acceptance-Rejection Method

Another relatively straightforward method to sample from a distribution is the acceptance rejection or rejection sampling method [95]. In its simplest form, one generates samples  $x$  from a uniform distribution and "accepts" them with the corresponding probability  $g(x)$  from the PDF one wants to sample from. The accepted samples then follow the desired distribution. Figure 4.2a shows an illustration of this process.

The main advantage of this method is that the only demand to the PDF is that one has to be able to evaluate it at any given point. This makes this method a lot more applicable for complicated distributions than the inverse transform method. However, the weakness of rejection sampling lies in the efficiency. Depending on the distribution at hand, rejection rates can be very high, and in extreme cases thousands of random number generations as well as function evaluations can be required to obtain a single sample. This can be somewhat mitigated by choosing an appropriate proposal function. If one is able to efficiently generate samples from a distribution that is similar to the desired one (usually via the inverse transform method), the



(a) Uniform proposal distribution. (b) More efficient proposal distribution.

Figure 4.2: Illustration of the acceptance rejection algorithm. Samples  $x$ , shown as dashed lines, are generated according to the proposal distribution (orange). The samples are accepted with a probability  $p(x)$  given by evaluating the PDF (blue) at  $x$ . The efficiency can be improved by choosing a proposal distribution that matches the PDF as good as possible.

acceptance rate and therefore the efficiency can be greatly improved. This process is shown in figure 4.2b. As can be seen, compared to a uniform proposal distribution, a lot more samples are generated where the PDF has high values, thereby increasing the acceptance rate.

In the source simulation, the acceptance rejection algorithm is currently not used due to these efficiency reasons. However, it could be the case in the future that changes in the descriptions of the cross sections (thus as combining different models for the ionization cross section, see section 3.5) might make the use of Markov Chains infeasible, leaving rejection sampling as the only option. Sampling with Markov Chains as well as its advantages and limitations will be covered in the following section.

### 4.2.3 Markov Chains

Generally, a Markov Chain is defined as a random process (as in, the production of a sequence of random results) where each result  $x_{i+1}$  directly depends on the previous results  $x_i$ , but not on the results before that [92]. One of the most simple examples for a Markov Chain is the one-dimensional integer random walk [96]. One starts at  $x_0 = 0$  and then takes a one-unit step randomly in positive or negative direction, resulting in either  $x_1 = 1$  or  $x_1 = -1$ . Repeating this process results in a Markov Chain, as the two possible results for  $x_{i+1} = x_i \pm 1$  always depend on the current position  $x_i$  but not on the results before, since it does not matter how one arrived there.

One way (among several others which will not be covered here) to use Markov Chains

to sample from a distribution is given by the Metropolis-Hastings algorithm, which is illustrated in figure 4.3 [92].

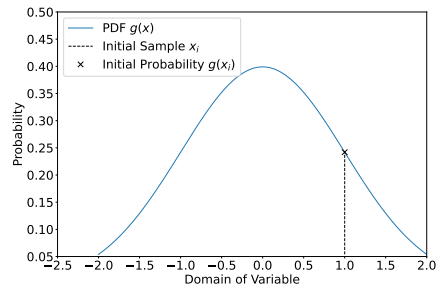
In this algorithm, the sample  $x_{i+1}$  is obtained by taking a step in a random direction from  $x_i$ , resulting in a proposal sample  $x_{\text{prop}}$ . The associated probabilities (i.e. function values of the PDF one wants to sample from)  $g(x_{\text{prop}})$  and  $g(x_i)$  are then compared. If  $g(x_{\text{prop}}) > g(x_i)$ , so the step was taken to a region of higher probability, the proposal is directly accepted as the new sample,  $x_{i+1} = x_{\text{prop}}$ . If however  $g(x_{\text{prop}}) < g(x_i)$ , the proposal is only accepted with a probability given by the ratio of the two PDF values  $g(x_{\text{prop}})/g(x_i)$ . In the case that the proposal is rejected, the initial sample is kept also as the new sample, i.e.  $x_{i+1} = x_i$ . The first sample  $x_0$  is normally obtained by making a guess and then running the Markov Chain for a while, discarding the samples obtained in this so-called "burn-in" period. This is done to ensure the Markov chain approaches the target distribution before the results are used.

One advantage of this sampling approach lies in its efficiency. Every time a step is taken or a proposal is made, a sample is guaranteed to be obtained. This results in a limited amount of random number generations and function evaluations per sample, similar to the inverse transform method. At the same time, Markov Chain sampling only requires being able to evaluate the PDF at any given point, making it suitable also for complicated distributions in a similar way as the acceptance rejection algorithm. On top of that, the method does not get significantly more complicated in higher dimensions, just the parameter space gets bigger. This allows to use Markov chain sampling for the two-dimensional ionization cross section.

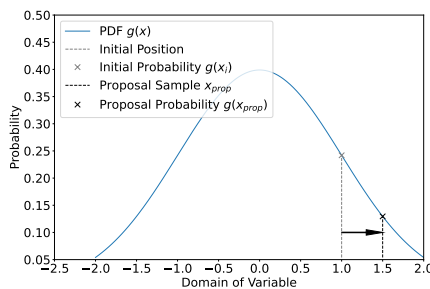
While the Metropolis-Hastings algorithm in that way combines several advantages of other sampling methods, it also has limitations, which partly play an important role when using it in an event-by-event Monte Carlo simulation.

Using the last sample to generate the next one of course results in a correlation between the two. This means that samples cannot be drawn on demand when a scattering happens, because an unphysical correlation between consecutive scattering events would be introduced. Therefore, a list of samples has to be prepared in advance, from which one then takes samples from varying locations. While simple in principle, this is challenging in a scattering simulation, since the distribution one wants to sample from changes based on the initial energy of the electron (see chapter 3). This was solved by generating several sample lists for a set of electron energies and then randomly choosing the appropriate list depending on the given electron energy. Details on this approach are covered in section 5.2.2.

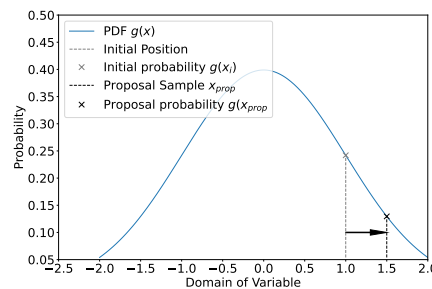
Another effect one has to keep in mind when sampling using Markov Chains is that the samples are generated by "walking" through the distribution. This means that if an insufficient number of samples is drawn, certain areas of the distribution may not be reached. This is especially apparent in cases with high variation in probab-



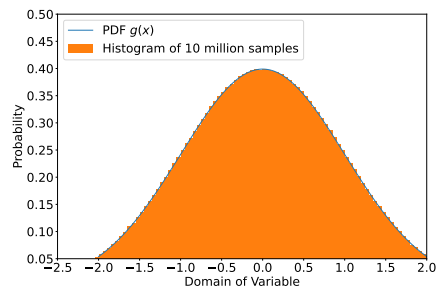
(a) PDF with an initial sample.



(b) Step to a higher probability.



(c) Step to a lower probability.



(d) Result.

Figure 4.3: Illustration of the Metropolis-Hastings algorithm. The goal is to generate samples distributed according to the PDF  $g(x)$  shown in blue. One starts at a known initial sample  $x_i$  with probability  $g(x_i)$  (a). From there, one takes a step in a random direction (in one dimension, either to the left or right) to a proposal sample  $x_{prop}$  associated with probability  $g(x_{prop})$ . If  $g(x_{prop}) > g(x_i)$ , the new sample is accepted (b). If not, it is only accepted with a probability  $g(x_{prop})/g(x_i)$  (c). If the proposal is rejected, one keeps the sample  $x_i$  again ( $x_{i+1} = x_i$ ). Repeating this many times results in samples distributed according to the PDF.

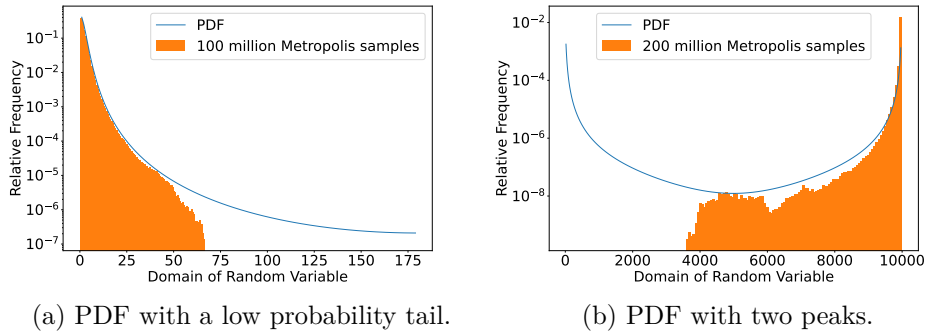


Figure 4.4: Illustration of the effect of an insufficient number of samples for PDFs sampled with Markov Chains. On the left, a low probability tail is not adequately represented for the number of samples. On the right, a second region of high probability is not reached because the Markov Chain did not "overcome" the region of low probability in between.

ility values, such as differential cross sections, which can vary over several orders of magnitude. Figure 4.4 illustrates the effects this can have.

In the plot 4.4a, one can see that an area of low probability is underrepresented by the Markov Chain samples. Although  $10^8$  samples are drawn, even regions with a probability of  $>10^{-6}$  have no samples, because the Markov Chain has not explored those areas yet. This is even more severe if one has a distribution with more than one region of high probability separated by a low probability region, as shown in plot 4.4b.

An obvious, brute force way to overcome this is by just generating enough samples that the entire spectrum is covered. While it is not easy to assess how much "enough" is for a given distribution and this approach might be impractical for applications where not many samples are needed, it actually works in the context of the full simulation of the source for the keV sterile neutrino search. The number of electrons that are planned to be simulated the exceeds the span of values that the cross sections take by several orders of magnitude (see chapter 3 and section 4.1). Hence, convergence of the Markov Chains is given. However, in order to make the simulation suitable for other applications and tests with less statistics, it is still worthwhile to look at techniques to mitigate the issue.

A key optimization parameter of the Markov Chain is the step size  $\epsilon$ . If  $\epsilon$  is too large, steps to low probability regions will be frequent, resulting in a low acceptance rate and consequently only little or slow movement through the spectrum. Too small steps however also cause a slow convergence, since the spectrum is essentially explored in a random walk. A lower bound on the number of steps  $N$  it takes to

explore a distribution of length  $L$  (range of the sample values) with a random walk of step size  $\epsilon$  and an acceptance rate  $f$  is given by

$$N \simeq \frac{1}{f} \left( \frac{L}{\epsilon} \right)^2 \quad [92]. \quad (4.4)$$

An optimized convergence therefore is found for a step size  $\epsilon$  that balances a good acceptance rate while not being too small. An example for the impact of different step sizes is shown in figure 4.5.

One million samples of the distribution

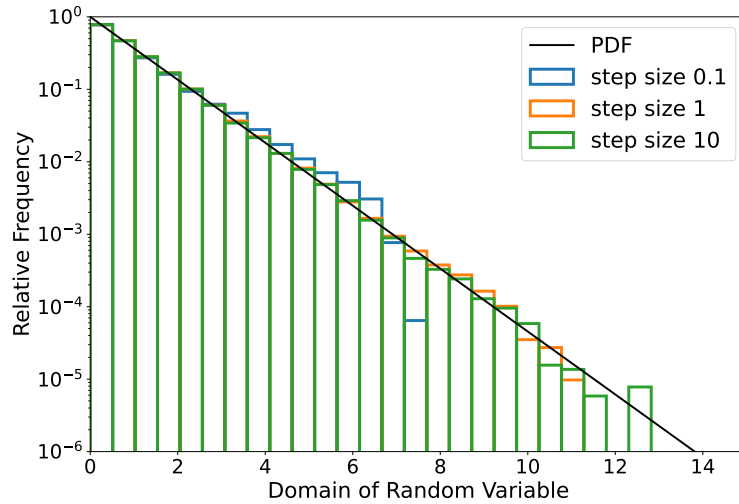
$$g(x) = \exp(-x), \quad x \in [0, 20] \quad (4.5)$$

were generated with a step size uniformly sampled between 0 and three different maximum values (0.1, 1 and 10). The average step size is then half that maximum, i.e. 0.05, 0.5 and 5. The exponential function was chosen because it has a variation over several orders of magnitude like the cross sections (see previous chapter) and can serve as a good indicator of how far the Markov Chain can explore the low probability region for a given number of samples. From the acceptance rates of the sampling, one can calculate the parameter  $N$  as given by eq. (4.4). The results are given in table 4.1.

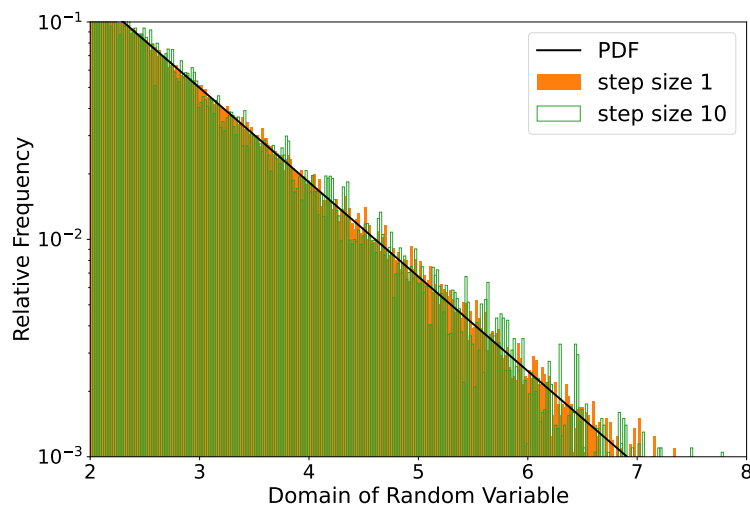
maximum step size $\epsilon$	acceptance rate $f$	$N$
0.1	0.95	170000
1	0.63	2500
10	0.10	160

Table 4.1: Acceptance rate  $f$  and convergence parameter  $N$  for different step sizes.

It is immediately clear that  $N$  really is only a lower bound on the number of steps that have to be taken to get through the spectrum, since none of the three sample sets cover the entire expected range of values even for a million samples. Plot 4.5a shows a histogram of the sample sets together with the PDF. One can see that the smallest step size sampling only covers a much smaller part of the distribution than the other two, which is consistent with the very large  $N$ . Step size 1 and step size 10 seem to perform similarly, with the larger step size sampling reaching values a little further into the spectrum, even (barely) reaching the  $10^{-6}$  probability region. However, the large step size comes with a different issue, with appears when looking at histograms with a finer binning, as displayed in figure 4.5b. There, one can see that the step size 10 sample set displays a much larger variation between bins than the step size 1 set. This means a detailed optimization of the step size should also take into account to what precision one needs the samples to be well distributed. Within this thesis, only a rough comparison was made to choose appropriate bin sizes



(a) Sampling with different step sizes.



(b) Zoom with finer binning.

Figure 4.5: Illustration of a different choice of Markov Chain step size. Maximum step sizes of 0.1, 1 and 10 were chosen to generate one million samples each of the function  $g(x) = \exp(-x)$  between 0 and 20. The smallest step size samples a significantly smaller part of the spectrum (a), while the largest one gets the furthest, but exhibits higher variation when looking at a finely binned histogram (b).

for the cross sections. A more detailed optimization could be worthwhile though, since the quality of the samples for a given statistics can potentially be significantly improved. On top of this simple optimization of the step size, several techniques exist to improve the convergence by reducing the random walk behaviour [92], for example using a non-constant step size, but have not been studied in detail in the context of this thesis. An exploration and detailed optimization might be done in the future.

#### 4.2.4 Comparison of Sampling Methods

While a lot of advantages and limitations of different sampling methods have been discussed in principle so far, it is of course of interest to see if these principles hold up in real-world scenarios. For this purpose, the inverse transform, acceptance-rejection (with and without efficient proposal distribution) and Markov Chain methods were applied to draw samples from the same distribution. Again, the exponential function from eq. (4.5) was used for this purpose. It was chosen again because it mimics the variation of the cross sections over several orders of magnitude well, onbut also because it is one of the few distributions for which the inverse transform method is possible.

Analogous to the sampling of scattering lengths as described by eq. (4.3), samples  $x$  of the PDF can be drawn by sampling  $P \in [0, 1]$  uniformly and transforming it by

$$x = -\ln(1 - P). \quad (4.6)$$

As a proposal distribution for the efficient rejection sampling, the function  $g_{\text{prop}}(x) = \frac{1}{2} \exp(-\frac{x}{2})$  was used, which can be sampled from using

$$x = -2 \ln(1 - P). \quad (4.7)$$

For the Markov Chain, the step size was uniformly sampled between 0 and 1. Figure 4.6 shows a histogram of one million samples obtained using each of the four methods.

One can see that all methods match the PDF well up to  $x$  values of about 10, when deviations start to happen due to low statistics. Even if only by a little, the Markov Chain samples stop earlier in the spectrum, as the Metropolis algorithm did not "walk" further. Table 4.2 compares the computing time to generate 10 million samples using the different methods, along with the acceptance rate (if applicable).

Note that the times stated here are not representative of sampling times in the simulation. This comparison was written in Python (as opposed to the simulation which is written in C++) and without any recording or other handling of the obtained samples, which significantly slows the code.

With this in mind, one can extract some information from these numbers. Firstly and unsurprisingly, the inverse transform method is the fastest, requiring only a

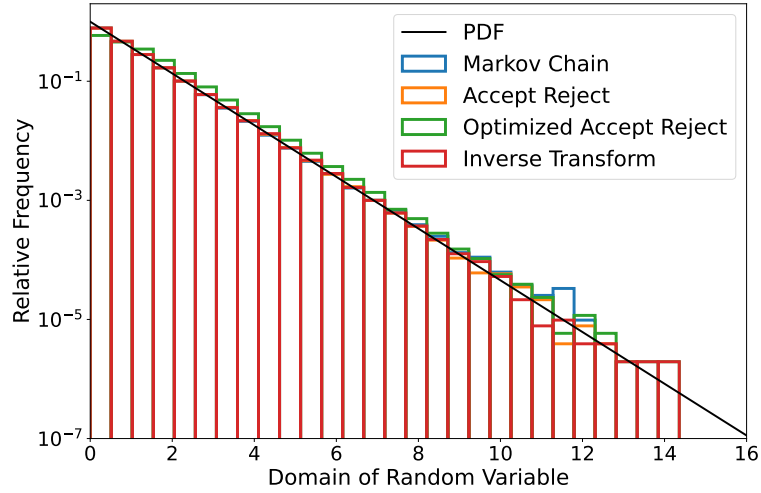


Figure 4.6: Histogram of 1 million samples of the PDF  $g(x) = \exp(-x)$  obtained using Markov Chains, rejection sampling and the inverse transform method.

method	computing time in seconds	acceptance rate
Markov Chain	30	1
Acceptance Rejection	323	0.050
Optimized Acceptance Rejection	53	0.75
Inverse Transform	6	1

Table 4.2: Comparison of computing time and acceptance rate of generating 10 million samples with different methods.

single random number and a function evaluation to generate a sample. The slowest of the four is the simple acceptance rejection method, which is due to the low acceptance rate of 0.05. This can be vastly improved by using a good proposal distribution. In the example here, it increased the acceptance rate to 0.75, resulting in a similar computing time to the Markov Chain. This means that if a good proposal distribution can be found, similarly efficient performance to the Markov Chain method is possible. However, for the cross sections, this is far from trivial since those are partly complicated functions with structures like the Bethe ridge which are not easy to mimic with a function with an analytically invertible integral (see chapter 3 in general and figure 3.4 for the specific example). It might be of interest though to do a detailed investigation on suitable proposal distributions, since a rejection sampling implementation that performs similarly efficient as a Markov Chain would be more

convenient to use regarding the ability to draw samples on demand, as described in the previous section. The same holds for the inverse transform method, where a detailed exploration of using numerical integration and inversion to draw the samples could potentially also result in competitive efficiency.

Knowing the physics in form of the scattering cross sections as well as ways to sample from them are the most important ingredients to develop a Monte Carlo simulation for scattering in the WGTS. How exactly this is applied is covered in detail in the next chapter.



# Chapter 5

## Scattering Simulation

As established in the previous chapters, a Monte Carlo simulation describing the scattering of electrons in the KATRIN WGTS has been developed in the context of this thesis. It uses Markov Chains to generate random samples from the differential scattering cross sections of electrons on molecular tritium and was developed with efficiency as a primary goal. The purpose of this chapter is to explain in detail its features and working principle.

Section 5.1 will give an overview of the working principle of the simulation, while section 5.2 will provide information on technical details necessary to ensure an efficient and functional simulation.

### 5.1 General Working Principle

The main purpose of the simulation is to describe how electrons are influenced by scattering on tritium molecules. For given a set of input parameters of an electron, the simulation provides a set of output parameters with which the electron exits the source. Three parameters are sufficient to describe the kinematic properties of an electron in the context of this simulation:

- The kinetic energy  $E$  is relevant as the cross sections depend on it. Also, it is arguably the most important output parameter, since it will be crucial for the sterile neutrino search to know how much energy the electrons lose in the source.
- The angle towards the beamline (i.e. symmetry axis)  $\theta$  is the second important output parameter. It determines if the electron leaves the source towards the rear wall or the detector and at what angle the electron will arrive there. On top of that,  $\theta$  determines how much distance an electron effectively travels through the source. The closer  $\theta$  is to  $90^\circ$ , the larger the effective length of the source  $d_{\text{eff}}$  becomes with respect to the actual length  $d$ :

$$d_{\text{eff}} = \frac{d}{\cos(\theta)}. \quad (5.1)$$

- The location  $z$  describes where the electron is in the source. It was chosen to use a coordinate system in which the tritium density is constant. This is possible if one assumes that, aside from the amount of tritium, there is no other dependency of the kinematic parameters on the physical location of the electron. The inherent limitations of that choice will be discussed in section 5.2.6. In this coordinate system,  $z$  can take values between 0 and 1 and thus describes the fraction of tritium gas between the rear wall and the electron (i.e. "behind" the electron if it flies towards the detector). This has the advantage that the only parameter required to be known about the source is the column density  $\rho d$ . The physical dimensions and the spatial density distribution are irrelevant.

A visualization of the coordinate definition as well as the working principle of propagating electrons through the source is shown in figure 5.1.

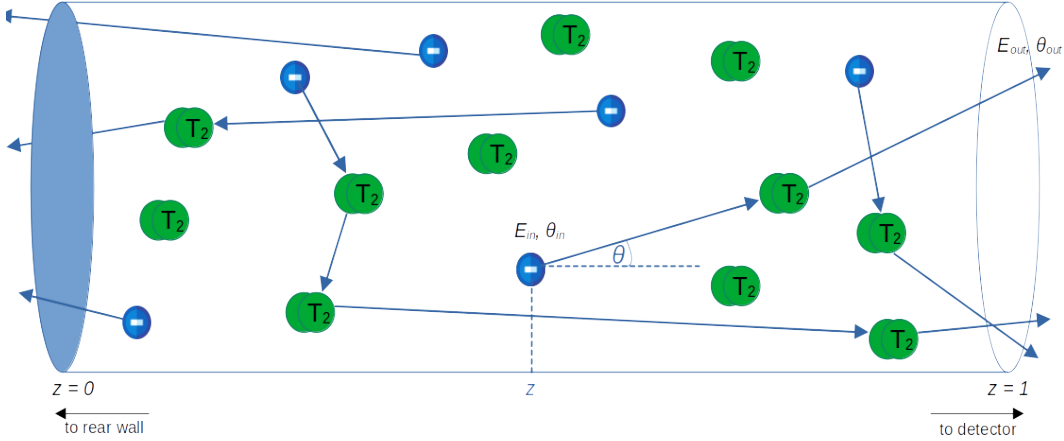


Figure 5.1: Visualization of the simulation working principle. Electrons are created at a location  $z$  with an energy  $E_{in}$  and angle  $\theta_{in}$ . Then, in a loop, scattering lengths are drawn and compared to the effective distance the electron can still travel in the source. For every scattering that happens, energy and angle are adjusted by drawing samples from the appropriate differential cross sections. The loop is broken when a scattering length is drawn that exceeds the remaining distance in the source. The current parameters  $E_{out}$ ,  $\theta_{out}$  are recorded and the next electron is created.

The process begins by creating an electron with initial parameters  $E_{in}$ ,  $\theta_{in}$  and  $z_{in}$ .  $E_{in}$  can in principle be sampled from any distribution (that one knows how to sample from, see chapter 4), but typically, the focus is on either the response to monoenergetic electrons, or electrons from the tritium decay and the values of

$E_{\text{in}}$  are generated accordingly. The angle  $\theta_{\text{in}}$  is typically either set to 0, in order to simulate an Electron gun (E-gun) measurement scenario where electrons enter the source from the side, parallel to the beamline, or  $\cos(\theta_{\text{in}})$  is uniformly sampled in order to model the isotropic tritium decay. Similarly,  $z_{\text{in}} = 0$  for an E-gun scenario, while uniform sampling between 0 and 1 would be used for an isotropic decay.

Once the electron is created, a "scattering length"  $x$  the electron travels before it scatters is determined, as described by equation (4.3). This length is compared to the distance the electron can still travel before it leaves the source. If  $x$  is smaller than that distance, a scattering occurs, and  $E$  and  $\theta$  are adjusted by drawing samples from the differential cross sections. Then,  $z$  is changed to the location where the scattering happened, and the next scattering length is drawn. These steps are repeated until a scattering length exceeds the remaining distance in the source. In that case, the next scattering would occur outside of the source, where no tritium is left to scatter from. The output values  $E_{\text{out}}$  and  $\theta_{\text{out}}$  of the electron are then recorded, and the next electron is generated.

Using this method, the electron is moved from one scattering to the next. This differs significantly from the approach taken in KASSIOPEIA, where electrons are propagated with a fixed step size, and each step involves checking for a scattering event [49].

The approach taken here is therefore more efficient, as only as many steps as scatterings are necessary, whereas KASSIOPEIA potentially requires many more steps. However, KASSIOPEIA also allows for tracking the physical movement of the electron in the electromagnetic fields in the source, which is not possible with the simulation developed here.

The next section will provide more detail on several key aspects of the simulation that were mentioned here.

## 5.2 Technical Details

While an overview of the simulation working principle has been given in the previous section, several points mentioned there require a more concrete and detailed explanation. This will be provided in the following. Section 5.2.1 will explain how the location of the next scattering is determined along with how the decision which process happens is made. Then, section 5.2.2 will show how the lists of Markov Chain samples are obtained and used. These are then needed to apply parameter changes when a scattering happens, covered in the following section 5.2.3. In ionization scattering processes, secondary electrons are produced. How they are dealt with will be shown in section 5.2.4. Details on the parameters that can be recorded when electrons leave the source and the methods used to record them will be provided in section 5.2.5. Finally, section 5.2.6 will explain the limitations of the simulation.

### 5.2.1 Determination of the next Scattering

After creating an electron, the first step of the simulation is to draw a length  $x$  the electron travels until it scatters. This process is described by equation (4.3). As previously explained in section 3.1, the values  $x$  takes depend on the mean free path

$$\lambda = \frac{1}{\rho \cdot \sigma},$$

which itself depends on the particle density  $\rho[\frac{1}{\text{m}^3}]$  and the total scattering cross section  $\sigma[\text{m}^2]$  and thus has a unit of meters. In coordinates with constant source density, one replaces  $\rho$  by the column density  $\rho d[\frac{1}{\text{m}^2}]$ , resulting in a dimensionless  $\lambda$ . Sampling using eq. (4.3) then results in  $x$  values in the correct coordinates, since  $\lambda$  is effectively expressed in units of the source length  $d$ . The value used for  $\sigma$  is given by the sum of the total inelastic and elastic cross section,  $\sigma_{\text{el}} + \sigma_{\text{inel}}$ , as described in section 3.2.

Once generated,  $x$  is compared to the remaining distance  $l_{\text{eff}}$  the electron can travel in the source before leaving, which depends on whether the electron is moving towards the detector ( $\cos(\theta) > 0$ ) or the rear wall ( $\cos(\theta) < 0$ ):

$$l_{\text{eff}} = \begin{cases} \frac{1-z}{\cos(\theta)} & \text{if } \cos(\theta) > 0 \\ \frac{z}{\cos(\theta)} & \text{if } \cos(\theta) < 0. \end{cases} \quad (5.2)$$

If  $x < l_{\text{eff}}$ , a scattering occurs within the source. The total cross sections of the individual processes (elastic, ionization and excitation, see chapter 3) are then evaluated for the current electron energy  $E$ . One of the processes is randomly determined with the cross sections serving as the probability. Once the process is known, the parameters of the electron are appropriately adjusted, which is covered in the next sections.

If  $x > l_{\text{eff}}$ , the next scattering would only occur once the electron is already outside the source. The electron therefore leaves without another scattering event. Its final parameters are then recorded as described in section 5.2.5, and one continues with the next electron.

### 5.2.2 Generation and Utilization of the Sample Lists

It has been established in section 4.2.3 that Markov Chains provide an efficient way to draw samples from a distribution, with the requirement that sample lists have to be prepared in advance in order to avoid correlation between subsequent scatterings. This poses a challenge, since the distribution one wants to sample from does not stay the same but is dependent on the electron input energy (see chapter 3). Therefore, it was chosen to prepare sample lists for a set of input energies  $E_i$ ,  $i = 0, \dots, n$ . If an

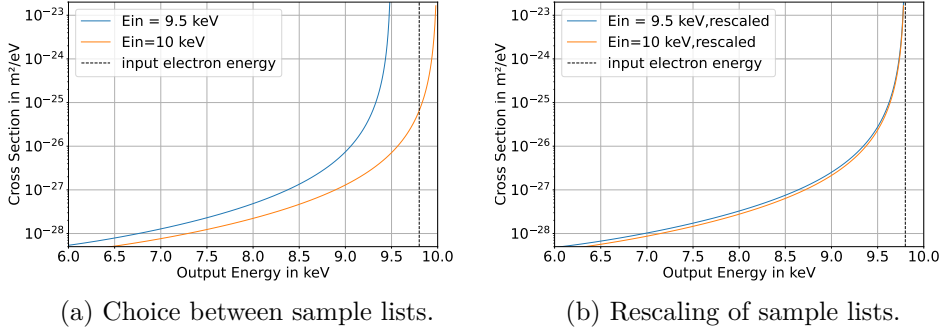


Figure 5.2: Example of the process of choosing between sample lists. An electron of energy  $E = 9.8$  keV scatters, but sample lists only exist for  $E_i = 9.5$  keV and  $E_{i+1} = 10$  keV (a). A sample from list  $i$  is used with a probability of 0.4, a sample of list  $i + 1$  with probability 0.6, as given by eq. (5.3). In either case, the sample that is drawn is rescaled by a factor of  $\frac{E}{E_{i/i+1}}$  to match the electron input energy (b).

electron of energy  $E$  with  $E_i < E \leq E_{i+1}$  scatters, one chooses randomly one of the two lists:

$$\text{sample taken from list} \begin{cases} i & \text{with probability } \frac{E_{i+1}-E}{E_{i+1}-E_i} \\ i+1 & \text{with probability } \frac{E-E_i}{E_{i+1}-E_i} \end{cases} \quad (5.3)$$

That way, the closer  $E$  is to a sample list energy, the more likely it is to choose a sample from that list. For generating angle samples, this method works well as described here. However, for modelling a continuous energy loss spectrum as given by the ionization scattering, an additional step is necessary: since the cross sections provide an output energy spectrum for a given input energy, this spectrum has to be rescaled to the energy of the given electron. Otherwise, unphysical results would occur: if the sample list  $E_{i+1} > E$  is chosen, the electron could "gain" energy, while for the smaller energy list  $E_i < E$ , the electron energy loss would be increased by  $E - E_i$ . An example for choosing between lists and this rescaling is shown in figure 5.2.

So far, no detailed study has been conducted on how accurately this method retrieves the correct distribution as well as its dependency on the bin width (i.e. the energy difference of the sample lists). This is however planned for the future. For the results that are shown in the next chapter, a bin width of 100 eV was used. For the Markov Chain sampling, the maximum energy step size was also chosen to be 100 eV. For the angle,  $5^\circ$  was used as maximum step size. In the burn-in phase, the first 10000 samples were discarded.

Once the appropriate list is chosen, a sample is taken from it from a location determined by a sample indicator parameter  $i$ . After the sample is taken, a random value (currently, uniformly between 10000 and 50000) is added to  $i$ , in order to get to a different location in the list for the next sample. This value was chosen to be on the same order of magnitude as the parameter  $N$ , as described by eq. (4.4). The samples generated in this way are then used to change the parameters of the electron when a scattering happens, which will be covered in the next section.

### 5.2.3 Modification of Electron Properties

Once the samples are picked from the appropriate list, the electron properties are updated. For the energy  $E$ , this is straightforward: the current energy is just replaced by the output energy provided by the sample drawn. The location  $z$  is adjusted by adding the scattering length  $x$  to the current location while accounting for the angle  $\theta$ :

$$z_{\text{new}} = z_{\text{old}} + \frac{x}{\cos(\theta)}. \quad (5.4)$$

For the angle  $\theta$  itself, an extra step is necessary: since the KATRIN beamline is cylindrically symmetric, the angle towards the beamline is sufficient to describe the electron direction, i.e. the azimuthal angle is irrelevant. The scattering processes modelled in the simulation are also cylindrically symmetric with respect to the initial electron direction of momentum, meaning no azimuthal angle  $\phi$  is preferred. However, since the electron momentum and the beamline are rotated with respect to one another by the initial electron angle  $\theta_{\text{old}}$ , the value of  $\phi$  plays a role in determining the new angle  $\theta_{\text{new}}$ . This relation is described by:

$$\cos(\theta_{\text{new}}) = \cos(\theta_{\text{old}}) \cos(\theta_{\text{scat}}) + \sin(\theta_{\text{old}}) \sin(\theta_{\text{scat}}) \cos(\phi), \quad (5.5)$$

where  $\theta_{\text{scat}}$  describes the polar angle sample, and the azimuthal angle  $\phi \in [0, 2\pi)$  is drawn uniformly.  $\phi$  is chosen such that  $\phi = 0$  corresponds to a scattering "towards the beamline":

$$\cos(\theta_{\text{new}}) = \cos(\theta_{\text{old}}) \cos(\theta_{\text{scat}}) + \sin(\theta_{\text{old}}) \sin(\theta_{\text{scat}}) = \cos(\theta_{\text{old}} - \theta_{\text{scat}}), \quad (5.6)$$

while  $\phi = \pi$  describes a scattering "away from the beamline":

$$\cos(\theta_{\text{new}}) = \cos(\theta_{\text{old}}) \cos(\theta_{\text{scat}}) - \sin(\theta_{\text{old}}) \sin(\theta_{\text{scat}}) = \cos(\theta_{\text{old}} + \theta_{\text{scat}}). \quad (5.7)$$

This process of including  $\phi$  corresponds to a rotation along the initial direction of the electron (described by  $\theta_{\text{old}}$ ), as visualized in figure 5.3.

In an ionization scattering processes, additionally to the adjustment of the primary electron parameters, a secondary electron is created. The handling of this process is covered in the next section.

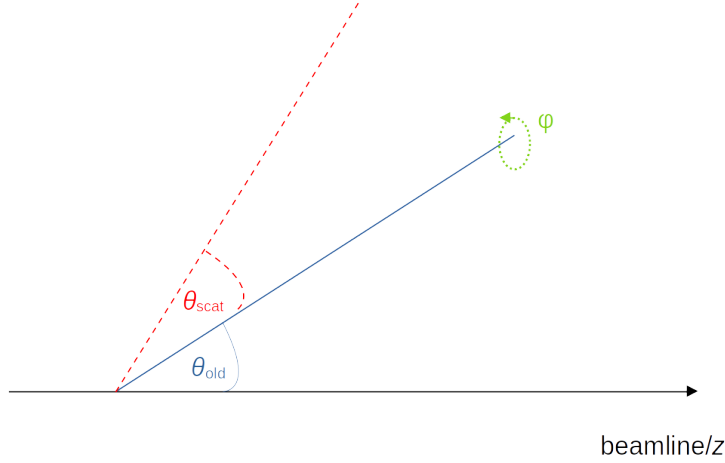


Figure 5.3: Visualization of the addition of angles in a scattering process. Eq. (5.5) corresponds to a rotation of the momentum transfer vector (described by  $\theta_{\text{scat}}$ ) around the initial electron momentum vector ( $\theta_{\text{old}}$ ), here for a rotation angle of  $\phi = \pi$ , corresponding to a scattering away from the beamline as described by eq. (5.7).

#### 5.2.4 Secondary Electrons

As established in section 3.2, ionization is the most dominant of the modelled scattering processes. Therefore, a lot of secondary electrons are created in the source that can potentially reach the detector and therefore need to be included in the simulation.

This is done by appending the properties of the secondary to a list anytime that an ionization scattering happens. The parameters are determined as described in section 3.5: the energy is calculated using eq. (3.16), while the angles  $\theta_{\text{scat},2}$  and  $\phi_2$  are determined assuming purely mechanical conservation of momentum between the primary and secondary angle [97]:

$$\theta_{\text{scat},1} + \theta_{\text{scat},2} = \frac{\pi}{2}, \quad \phi_2 = \phi_1 + \pi. \quad (5.8)$$

Plugging these relations into eq. (5.5) and applying trigonometric identities, one can derive a formula for the angle of the secondary  $\theta_{\text{new},2}$ , depending on the parameters of the primary electron:

$$\cos(\theta_{\text{new},2}) = \cos(\theta_{\text{old},1}) \sin(\theta_{\text{scat},1}) - \sin(\theta_{\text{old},1}) \cos(\theta_{\text{scat},1}) \cos(\phi_1). \quad (5.9)$$

After all the primary electrons are simulated, the list of secondaries is iterated over, creating electrons with the saved parameters and propagating them through the source. If these electrons create secondaries themselves, these are appended to the list and eventually also simulated until all electrons have left the source.

As explained in section 3.5, only electrons with an energy above the retarding energy of the main spectrometer will be detected. That means that only secondary electrons receiving a significant amount of energy from the primary are contributing to the detected spectrum. For the source simulation this is beneficial for two main reasons: firstly, it allows for the primary-secondary momentum conservation approximation, as discussed in section 3.5. Secondly, there is no need to simulate electrons with an energy lower than that threshold. Therefore, electrons with an energy lower than a parameter  $qU$  (representing the main spectrometer potential energy) are removed from the list of secondaries. Setting  $qU$  to a value  $\gtrsim 1$  keV was found to greatly improve the efficiency of the simulation, since the total scattering cross section diverges for  $E \rightarrow 0$ , as shown in equations (3.6) and (3.8). Therefore, low energy secondaries would scatter extremely frequently, requiring substantial computation time.

When the list of (relevant) secondaries is fully simulated, all the desired output parameters are recorded. This process is explained in the next section.

### 5.2.5 Output Parameters

While the main output parameters of the simulation are the outgoing electron energy and angle, other quantities can also be of interest. The parameters that can currently be recorded are the initial properties of the electron (energy  $E_{\text{in}}$ , angle  $\theta_{\text{in}}$  and location  $z_{\text{in}}$ ), the final energy  $E_{\text{out}}$  and angle  $\theta_{\text{out}}$  and the number of scatterings. The latter is recorded in total ( $n_{\text{tot}}$ ) as well as resolved by the type (ionization  $n_{\text{ion}}$ , excitation  $n_{\text{exc}}$  and elastic  $n_{\text{el}}$ ).

These parameters are stored in vectors that get appended for each electron that is simulated and then copied to text files once the simulation is completed. That means that the event by event data is preserved in the output. This allows for detailed studies and understanding of the processes in the source as well as flexibility in terms of e.g. binning when comparing the results to other simulations (see chapter 6). However, this type of data recording also hampers efficiency and results in large output files, making it unfeasible for very high statistics simulations. For simulations towards the TRISTAN statistics, an alternative output format will have to be added, such as directly histogramming the data.

The limitations of the output approach currently used as well as the simulation in general will be discussed in more detail in the next section.

### 5.2.6 Limitations

The objective of this thesis was to develop a Monte Carlo simulation that is relatively simple, but efficient. The actual speed at which electrons can be simulated depends significantly on the settings (such as  $qU$  or the output parameters one wants to know, see the previous sections), but generally lies in the order of magnitude of  $\mathcal{O}(10^7 \text{ electrons/core}/100 \text{ seconds})$ .

Optimizing the efficiency of the simulation results in limitations in other aspects. Regarding the modelling of the physical processes, the most important limitation is that the actual trajectory of the electrons is not tracked. As described in section 5.1, the whole simulation is performed in a rather abstract coordinate system where the source density is constant and neither the tritium density distribution nor the actual dimensions of the WGTS are relevant. This approach is based on the assumption that the magnetic fields in the source just perfectly guide the electrons on spiral trajectories towards the pumping sections. In reality, this is of course an approximation. A simulation of the magnetic field distribution of the WGTS is shown in figure 5.4.

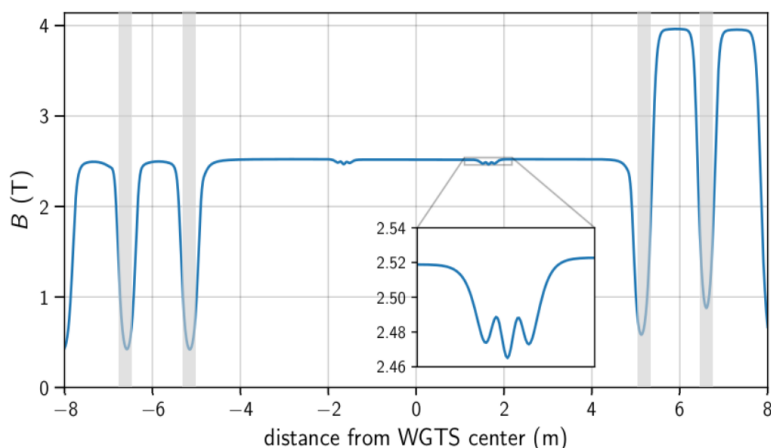


Figure 5.4: Simulation of the magnetic field strength on the beamline axis in the WGTS. Between the pump ports marked in grey, the magnetic field is almost constant. However, there are small minima in which electrons can get trapped. Figure adapted from [47].

In this picture, it can be observed that while the magnetic field in the source is nearly constant, small inhomogeneities exist at the borders of the superconducting magnet coils. Also, not all the tritium is removed at the first pump ports, where the field strength drops much more significantly. Electrons created with a large angle towards the beamline in these regions are magnetically trapped until their angle

changes by scattering or non-adiabatic motion [47]. This effect has to be simulated in order to know the impact on the overall energy and angle distribution. Unfortunately, this is not easily possible with the current Monte Carlo simulation since the spatial density distribution needs to be known. However, it might be possible to simulate the magnetic trapping effect externally and feed the parameters with which the electrons exit the traps as input to the source simulation. Simulation of the magnetic trapping is possible within the KASSIOPEIA framework, for example. Most other limitations to the accuracy of the simulation are either related to uncertainties of the cross sections (covered in chapter 3) or the sampling (chapter 4 and section 5.2.2). A thorough investigation of the impact of these on the TRISTAN sensitivity will be performed in the future.

Other limitations of the simulation lie less in the accuracy of its results, but more in practical issues when using it. These arise mainly due to two reasons. Firstly, as has been covered in detail in section 4.2.3, Markov Chain sampling requires fewer function evaluations and is thus more efficient than the acceptance rejection method, at the cost of sample lists having to be prepared in advance.

Secondly, the recording of output parameters is done by copying a vector containing the results for all electrons to an output file. This was found to improve the efficiency of the code by a factor of  $\sim 10$  compared to directly writing the results for every single electron to a file. Both of these approaches greatly speed up the code, but at the expense of having to store large amounts of data in memory. This makes it impossible to run the simulation for a very large amount of electrons at once, the desired amount of statistics has to be reached by running many batches small enough for the memory to handle.

Ways to make the code less memory-intensive without sacrificing too much efficiency will be investigated and implemented in the future. This includes regularly saving the output data to a file to free memory space as well as the possibility of having the sample lists stored in an external file.

Having explained the working principle of the simulation in this chapter, the next chapter will focus on the first results obtained with it.

# Chapter 6

## Application and Results

While the main focus of this thesis was the development of the simulation, some first investigations have already been conducted. The results of these investigations will be shown in the following.

Generating monoenergetic electrons isotropically in the source gives a good first impression on how the energy and the angle of the beta electrons are generally affected by scattering in the source. This, along with a first comparison of the results of this simulation with the ones obtained with the code currently used to produce the scattering response matrices in TRModel is covered in section 6.1.

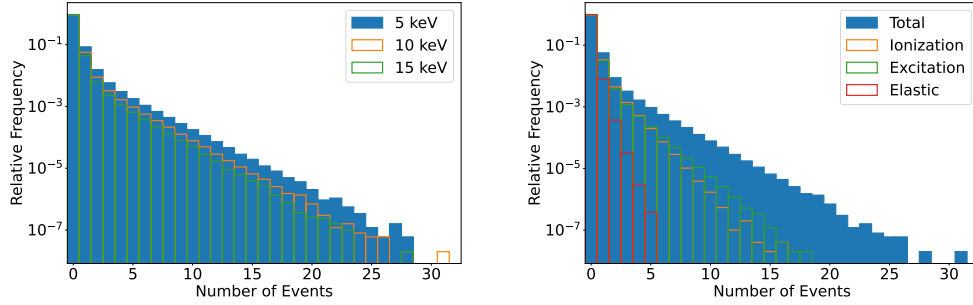
The simulation is also sufficiently versatile to be used for slightly different applications. In the KATRIN neutrino mass measurement, the determination of the energy loss function of the WGTS is an important part of the overall transmission function. The simulation could be used as a crosscheck for another prediction tool which gets compared to experimental data. The results of this will be shown in section 6.2.

### 6.1 Source Simulation for TRISTAN

First results of the code were obtained by defining a reference scenario for which monoenergetic electron with varying energy were generated uniformly and isotropically in the source. Comparing the input and output energy and angle in this setup, one can already see the general structure of systematic effects that scattering in the WGTS introduces to the tritium decay spectrum. This is covered in section 6.1.1. Section 6.1.2 will then show the results of a first comparison by A. Onillon of the simulation with results of the code generating the TRModel scattering response matrices.

#### 6.1.1 Investigation of Main Systematic Effects

In order to get a first impression of the main structural effects that scattering in the source has on the tritium spectrum as well as its overall impact, a preliminary simulation as been performed.  $5 \times 10^7$  electrons were created with an isotropic angle and location in the source, as described in section 5.1. This was done for



(a) Number of scatterings for different electron input energies. (b) Number of scatterings by type, for 10 keV electrons.

Figure 6.1: Histograms of the number of scattering events the generated electrons experienced before leaving the source. Comparing the histograms for different input energies, it can be seen that low energy electrons scatter more frequently (a). Resolving by scattering type, one can see that ionization and excitation are dominant over elastic scattering (b). Overall, most electrons do not scatter at all, but in a few cases, the electron scatters more than 20 times before leaving the source.

3 electron starting energies: 5, 10 and 15 keV, each at a source density of  $\rho d = 5 \times 10^{19}$  molecules/m<sup>2</sup>, which is 1% of the KATRIN nominal source density [43]. The energy cut-off was chosen as  $qU = 1$  keV.

A good overview of the impact of scattering in the source is obtained by looking at the number of times the electrons scatter before they exit the source. This is shown in figure 6.1.

It can be seen that most electrons leave the source without scattering at all. The total number of scatterings depends on the initial energy of the electrons and here ranges from 89% for 5 keV electrons to 94% for 15 keV electrons. This makes sense considering the mean free path of the electrons at these energies and this column density, given by eq. (3.2) are:

$$\lambda = \begin{cases} 16.5d & E = 5 \text{ keV} \\ 29.8d & E = 10 \text{ keV} \\ 42.2d & E = 15 \text{ keV}. \end{cases} \quad (6.1)$$

As described in section 5.2.1,  $\lambda$  is given in units of the source length  $d$ , so only electrons that effectively travel that length multiple times are likely to scatter. This is not the case for most electrons, resulting in a relatively low overall scattering probability. However, there are electrons created with an angle nearly perpendicular to the beamline. In that case the effective length they have to travel through the

source can become arbitrarily large, as described by eq. (5.1). These electrons can then scatter many times before leaving the source, resulting in the long tail that can be seen in the histograms.

Figure 6.1a shows that scattering is overall more likely for low energy electrons, as is expected from the total cross sections (see figure 3.1).

A further comparison with expectations can be done when resolving the number of scatterings by the scattering type, as shown in the plot 6.1b. There, one can see that ionization and excitation processes are a lot more likely than elastic scattering, which again matches the total cross sections shown in figure 3.1.

Another observation can be made here: based on the cross sections, ionization scattering is expected to be slightly more likely than excitation processes. This is reflected in the histogram for a small number of scatterings, but for electrons that scattered several times, excitation becomes more likely. This can again be explained by considering that electrons that scatter often do so because they have an angle towards the beamline close to  $90^\circ$ . When examining the angle distribution of excitation (figure 3.3a) and ionization scattering (figure 3.4), it is clear that a high scattering angle is far more likely in an ionization event. This means, that electrons that scatter via ionization often significantly change their angle, resulting in a much shorter effective source length and thus fewer further scattering events. Electrons that scatter via excitation on the other hand often only experience minimal angle changes and thus can experience several excitation scatterings without drastically reducing the effective source length.

While the number of scattering events provide some interesting insights, the energy and angular change induced by the scattering are more relevant in the framework of TRISTAN. The angular change due to scattering on 10 keV electrons is presented in figure 6.2.

Comparing the initial and final angle distribution, it can be seen that a significant change is only introduced for values around  $\cos(\theta) = 0$ , i.e. for electrons moving nearly perpendicular to the beamline. This is again due to the fact that most other electrons leave the source without scattering, and if they scatter, there is a priori no preference for a particular direction of angle change or a similar effect that would disturb the isotropic distribution. However, as discussed above, the closer an electron angle is to  $90^\circ$ , the longer the effective distance the electron travels through the source and thus the larger the probability to scatter becomes. Electrons are then much more likely to leave the source without scattering more often once their angle towards the beamline is smaller. Since for all scattering processes, small angle changes are the most probable, this is a very local effect in the distribution and results in the "valley" structure in figure 6.2b.

The other main output parameter of interest is the energy of the electrons. The final energy distribution for monoenergetic electrons of the three energies 5, 10 and 15 keV is shown in figure 6.3.

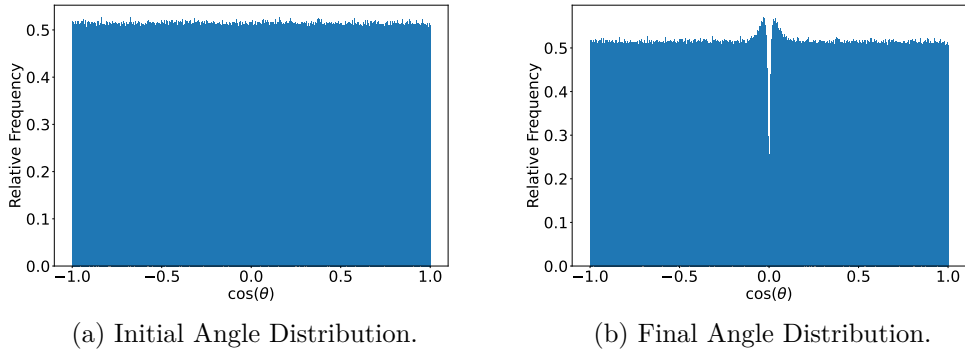


Figure 6.2: Effect of Scattering on the electron angle distribution, for 10 keV electrons. Electrons with an angle nearly perpendicular to the beamline travel a longer effective source length and are thus more likely to scatter. They are more likely to leave the source without further scatterings once their angle towards the beamline is smaller.

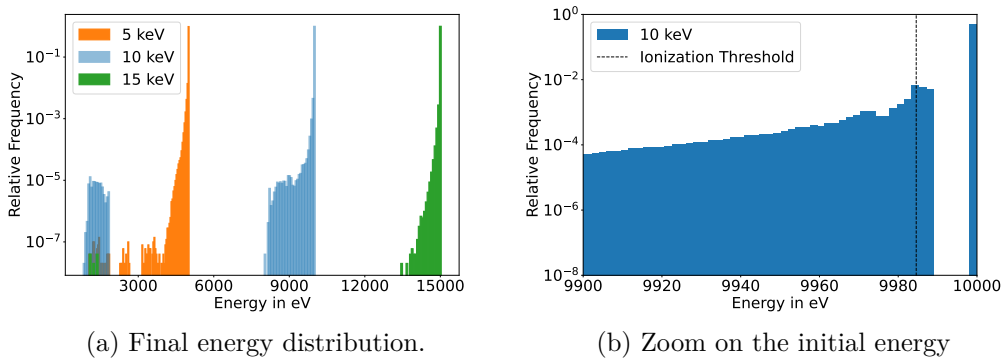


Figure 6.3: Final energy distribution of electrons of input energy 5, 10 and 15 keV, including secondary electrons with energies  $> 1$  keV (a). Also shown is a zoom on the initial energy for 10 keV electrons, revealing a gap caused by the minimum energy loss in excitation (12.7 eV) and ionization scattering (15.4 eV) (b).

The first observation one can immediately make here is that  $5 \times 10^7$  electrons are by far not enough to adequately model the entire energy distribution. A simulation with more statistics has been performed for the comparison with the TRModel, which will be covered in the next section. Despite the insufficient sampling, this first investigation contains some valuable information.

Firstly, one again finds that most electrons do not change their energy at all, which is consistent with the observation from the scattering statistics that most electrons leave the source without scattering.

Secondly, it can be seen that small energy losses are far more likely than large ones. This is expected, since the ionization cross section decreases steeply for higher energy losses while excitation losses in any case only happen on the order of  $\mathcal{O}(10 \text{ eV})$  (see chapter 3). The minimum energy loss in an inelastic scattering is 12.73 eV, given by the lowest electronic excitation state. This results in a characteristic "gap" between the electrons that inelastically scattered and the ones that did not, shown in the plot 6.3b. There, the impact of ionization processes setting in is visible as an increase of counts at the ionization threshold. Some other effects of the quantized energy losses can be seen near the initial energy, but are then washed out towards lower energies. A comparison of the results of this simulation with the source response given by the TRModel is covered in the next section.

### 6.1.2 First Comparison to TRModel results

While the general behaviour of the simulation is as expected, comparison to other data is crucial in order to adequately evaluate its correctness and precision. A preliminary comparison to the results of the source simulation used to produce scattering response matrices for the TRModel has been performed by A. Onillon. This simulation uses a binned convolution approach to model scattering in the source, as described in section 2.3.3. For the Monte Carlo simulation,  $5 \times 10^8$  electrons were generated, again isotropically in location and angle for electron energies of 5, 10 and 15 keV. The resulting event by event data was then binned to match the convolution data bin width of 100 eV for the energy and 0.04 (in units of  $\cos(\theta)$ ) for the angle. For the convolution, the source was divided into 5 slices.

Figure 6.4 shows the resulting energy distribution of both approaches.

It can be seen that even though the amount of electrons was increased by a factor of 10 with respect to the first investigation from the previous section, the energy spectrum is still not fully sampled. This makes a detailed investigation impossible. Therefore, running a simulation with a factor of about  $\sim 100$  more electrons is planned for the future.

What can be observed from the available data is that the general structure of the energy loss and angle change is similar, but significant differences exist. Aside from insufficient statistics from the Monte Carlo simulation, there are several possible

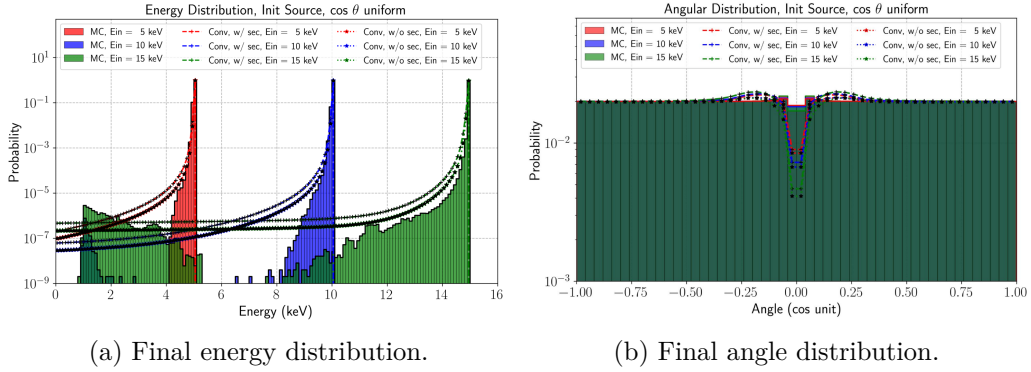


Figure 6.4: Comparison of the resulting energy and angle distributions of the Monte Carlo simulation and the convolution code. The latter is shown both for secondaries activated and deactivated. Plot by A. Onillon [98].

reasons for this. On the side of the Monte Carlo simulation, there are known possible inaccuracies related to either the cross sections and the sampling (see chapters 3, 4 and section 5.2.6) that could contribute to the difference. For the convolution code, the biggest uncertainty is likely introduced by the binning of the source location, the angle and the energy. As has been mentioned, a more thorough investigation involving significantly more statistics by the Monte Carlo simulation is planned for the future.

## 6.2 KATRIN Energy Loss Investigations

As discussed in section 2.2.6, scattering in the WGTS and the corresponding energy loss also play an important role in the neutrino mass measurement. In KATRIN, this is modelled by assuming that the probability of  $n$ -fold scattering by an electron is given by a Poisson distribution:

$$P_n(\mu) = \frac{\mu^n}{n!} \exp(-\mu), \quad (6.2)$$

where  $\mu = \rho d \sigma$  is the expected number of scatterings. The scattering response for an electron that scattered  $n$  times is obtained by convolving the energy loss function  $f(E)$  for a single scattering with itself  $n$  times. The energy loss function can be measured by shooting electrons through the source from the rear wall side with an E-gun [48].

The description by a Poisson distribution is based on the assumption that the probability to scatter stays constant, for different electrons as well as for a single electron while it travels through the source. However, there are several effects that can change

the scattering probability.

These effects relate to a change in the electron parameters, namely their energy and their angle towards the beamline. The energy has influence on the total cross section  $\sigma$ , and thus a different electron energy results in a different  $\mu$ . A varying electron angle changes the effective source length  $d_{\text{eff}}$  as described by eq. (5.1) and thus also changes  $\mu$ . Energy and angle can vary for two main reasons: Firstly, for two separate electrons, they can already be different when the electrons enter the source. Ideally, an E-gun produces electrons parallelly and at a perfectly constant energy, but in reality, a small fluctuation is expected. Secondly, those parameters are of course changed by the scattering itself.

In order to assess the impact of these effects, the Monte Carlo simulation can be used. For this purpose,  $5 \times 10^8$  electrons each have been simulated for three scenarios. The first one models an ideal egun, with electrons of energy  $E_{\text{in}} = 18575 \text{ eV}$  entering the source parallelly to the beamline ( $\theta_{\text{in}} = 0$ ) from the rear wall side ( $z_{\text{in}} = 0$ ). In the second scenario, a uniform variation between 0 and 60 eV was introduced to each electron's energy, and an additional uniform angle variation between 0 and  $5^\circ$  was added in the third one. The resulting number of inelastic scatterings were then compared to a Poisson distribution which was obtained by calculating  $\mu$  as the average number of scatterings per electron:

$$\mu = \sum_{n=0}^N n \cdot \text{counts}(n). \quad (6.3)$$

Here,  $\text{counts}(n)$  represents the number of electrons that scattered  $n$  times, and  $N$  is the highest number of scatterings that was observed. The results of this are shown in figure 6.5.

Plot 6.5a shows the number of inelastic scatterings in the case of the ideal E-gun together with the Poisson fit. In this representation, neither a deviation nor the error bars of the Monte Carlo data is visible. This changes when examining the relative difference between the simulation results and the Poisson fit, depicted in plot 6.5b. Here, one can see that there is a small, but significant deviation between the two. The error bars have been obtained by splitting the  $5 \times 10^7$  electrons into 50 "batches" of 10 million electrons each. The results for the 50 batches were then averaged and their standard deviation  $\sigma_{\text{std}}$  calculated. The error bars are then given by  $\sigma_{\text{std}}/\sqrt{50}$ . The uncertainty gets larger for a higher number of scatterings due to the lower statistics there (more scatterings are less probable, as shown by plot 6.5a). Comparing the three scenarios, it can be seen that they agree within the statistical uncertainty. This means that a change in starting parameters is not the main reason for the deviation from the Poisson behaviour, but rather the parameter change introduced by scattering. This small deviation on the order of  $\sim 1\%$  was also observed in energy loss simulations performed specifically for KATRIN [99]. Thus,

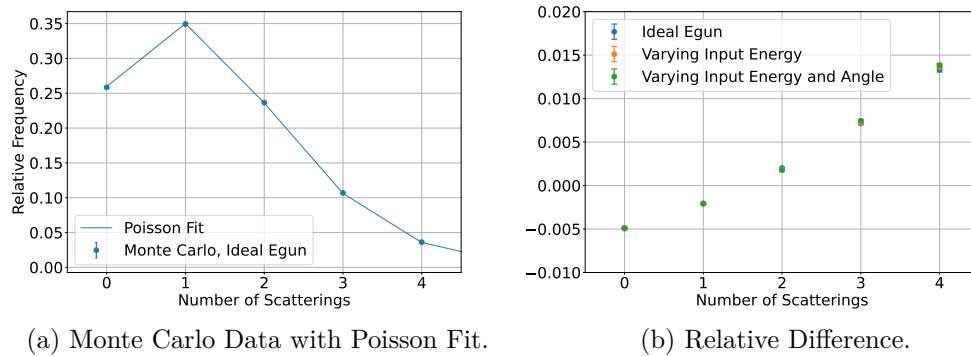


Figure 6.5: Comparison of Monte Carlo Data ( $5 \times 10^8$  electrons) to a Poisson fit, for the ideal E-gun case (18.575 keV electrons, parallel to the beamline)(a). For all three cases, the relative difference of the simulation data to the Poisson fit is shown (b). The error bars represent only the statistical fluctuation of the Monte Carlo data.

this small investigation also provided a good crosscheck for both simulations. While the first results of the source simulation look promising, a lot of improvements are still possible and much more testing will be required in the future. The next chapter will summarize some conclusions on the results already obtained and provide an outlook on further developments.

# Chapter 7

## Conclusion and Outlook

The goal of this work was to develop an efficient Monte Carlo simulation for electron scattering in the KATRIN tritium source. The first working version of this simulation has been completed. It incorporates the most important types of scattering (ionization, electronic excitation and elastic scattering) and is capable of simulating  $\mathcal{O}(10^7)$  electrons/core/100s by efficiently drawing samples from the differential cross sections using Markov Chains. The first results obtained show behaviour as expected and consistent with previous simulations in their general structure. However, significant quantitative differences exist which will be investigated in detail in the future.

The simulation still has a lot of room for improvement which can be split in two categories: improvements regarding the code and its efficiency and improvements regarding the physics.

Concerning the former, sampling is a point that needs to be further investigated. While the Markov Chains proved to be efficient and simple to implement, compromises needed to be made in order to make them suitable for this specific application. This involved having sets of sampling lists prepared in advance in order to account for changing distributions depending on the electrons' input energy. The bias introduced by this approximation remains to be studied and quantified in detail. Further optimizations may be necessary to reduce this bias to a non-relevant level. The Markov Chain method as well as the recording of output data have proven to be quite memory intensive. Future investigations will focus on optimizing these methods to reduce memory usage without compromising efficiency. This includes studying in detail if other sampling methods such as the optimized rejection sampling or the inverse transform method using numerical integration and inversion could be implemented in a way similarly efficient to the Markov Chain, eliminating the need for prepared sample lists.

Another way of further speeding up the simulation that is being considered is multi-threading and GPU computation, similarly to the existing convolution code simulation. In any case, further improvement is necessary since with the current efficiency, even on 1000 cores, about  $1 \times 10^{13}$  electrons could be simulated per day, making a simulation of  $10^{17}$  electrons infeasible.

Regarding improvements of the physics description of the simulation (namely, the cross sections), several possibilities are being considered. The main challenge is that literature on electron scattering in the relevant energy region is sparse for regular hydrogen molecules and even more so for tritium. Nonetheless, the ionization energy loss description could potentially be improved upon by using the BED model instead of the semiempirical cross section that is presently implemented. However, since the BED model does not provide an angle distribution, it would need to be combined with other methods. The feasibility of doing this while still maintaining efficient sampling needs to be investigated. Another possibility would be to explicitly perform the theoretical calculations specifically for KATRIN. This has already been done for the excitation case. The results of this will be implemented in the simulation in the near future.

On top of that, the uncertainties of the cross sections and their propagation need to be investigated in detail. How accurate these formulas are is a key information to evaluate how sensitive the experiment is to a keV sterile neutrino signal.

All these improvement ideas work towards the goal of having a simulation that is accurate as well as efficient enough to analyze TRISTAN data. To achieve this, detailed sensitivity studies have to be performed, which will be the first major application of the simulation.

# List of Acronyms

- $0\nu\beta\beta$**  Neutrinoless Double Beta Decay. 5–7
- BED** Binary Encounter Dipole. 40, 76
- CDF** cumulative distribution function. 44–46
- CMB** Cosmic Microwave Background. v, 6, 7
- CMS** Calibration and Monitoring System. 14
- CPS** Cryogenic Pumping Section. 14, 15
- DAQ** data acquisition. v, 23, 26
- DM** Dark Matter. v, 7, 9
- DPS** Differential Pumping Section. 14, 15
- E-gun** Electron gun. 59, 72–74
- FPD** Focal Plane Detector. 17, 23, 24
- GPU** Graphics Processing Unit. 28, 75
- KATRIN** KArllsruhe TRItium Neutrino. v, vi, 7, 9, 11–13, 15–23, 25, 38, 40, 43, 57, 62, 67, 68, 72, 73, 75, 76
- MAC-E Filter** Magnetic Adiabatic Collimation combined with an Electrostatic Filter. 12, 15, 16
- PDF** probability density function. 44–51, 53, 54
- PMNS matrix** Pontecorvo-Maki-Nakagawa-Sakata matrix. 4, 8
- SDD** Silicon Drift Detector. 23, 24

**SM** Standard Model of Particle Physics. v, 1, 3, 5, 8

**WGTS** Windowless Gaseous Tritium Source. 12–15, 19, 26–29, 43, 44, 55, 57, 65, 67, 72

**WIMPs** Weakly Interacting Massive Particles. v

## Bibliography

- [1] Tristram, M. et al. ‘Cosmological parameters derived from the final Planck data release (PR4)’. In: *AA* 682 (2024), A37. DOI: 10 . 1051/0004 - 6361/202348015.
- [2] Gianfranco Bertone, Dan Hooper and Joseph Silk. ‘Particle dark matter: evidence, candidates and constraints’. In: *Physics Reports* 405.5 (2005), pp. 279–390. ISSN: 0370-1573. DOI: <https://doi.org/10.1016/j.physrep.2004.08.031>.
- [3] The KATRIN Collaboration. ‘Direct neutrino-mass measurement with sub-electronvolt sensitivity’. en. In: *Nat. Phys.* 18.2 (Feb. 2022), pp. 160–166.
- [4] S Mertens et al. ‘Characterization of silicon drift detectors with electrons for the TRISTAN project’. In: *J. Phys. G Nucl. Part. Phys.* 48.1 (Jan. 2021), p. 015008.
- [5] W Pauli. ‘The proposal of the neutrino: Brief an die Gruppe der Radioaktiven’. In: *Pauli Letter Collection* (1930).
- [6] Enrico Fermi. ‘Versuch einer Theorie der  $\beta$ -Strahlen. I’. In: *Zeitschrift für Physik* 88.3 (1934), pp. 161–177.
- [7] Frederick Reines and CL Cowan Jr. ‘Detection of the free neutrino’. In: *Physical Review* 92.3 (1953), p. 830.
- [8] Gaillard Danby et al. ‘Observation of high-energy neutrino reactions and the existence of two kinds of neutrinos’. In: *Physical Review Letters* 9.1 (1962), p. 36.
- [9] K Kodama et al. ‘Observation of tau neutrino interactions’. In: *Physics Letters B* 504.3 (2001), pp. 218–224.
- [10] S N Gninenko, D S Gorbunov and M E Shaposhnikov. ‘Search for GeV-scale sterile neutrinos responsible for active neutrino oscillations and baryon asymmetry of the Universe’. In: *Adv. High Energy Phys.* 2012 (2012), pp. 1–17.
- [11] Chien-Shiung Wu et al. ‘Experimental test of parity conservation in beta decay’. In: *Physical review* 105.4 (1957), p. 1413.
- [12] Maurice Goldhaber, Lee Grodzins and Andrew W Sunyar. ‘Helicity of neutrinos’. In: *Physical review* 109.3 (1958), p. 1015.

- [13] Andrew J. Larkoski. *Elementary Particle Physics*. Cambridge: Cambridge University Press, 2019. ISBN: 9781108496988.
- [14] John N. Bahcall and Raymond Davis. ‘Solar Neutrinos: A Scientific Puzzle’. In: *Science* 191.4224 (1976), pp. 264–267. DOI: 10.1126/science.191.4224.264.
- [15] John N Bahcall, Neta A Bahcall and Giora Shaviv. ‘Present status of the theoretical predictions for the Cl-37 solar-neutrino experiment’. In: *Physical Review Letters* 20.21 (1968), p. 1209.
- [16] M Cribier et al. ‘Results of the whole GALLEX experiment’. In: *Nuclear Physics B-Proceedings Supplements* 70.1-3 (1999), pp. 284–291.
- [17] JN Abdurashitov et al. ‘Measurement of the solar neutrino capture rate in SAGE’. In: *Nuclear Physics B-Proceedings Supplements* 118 (2003), pp. 39–46.
- [18] C Arpesella et al. ‘Direct measurement of the  $^7\text{Be}$  solar neutrino flux with 192 days of Borexino data’. en. In: *Phys. Rev. Lett.* 101.9 (Aug. 2008), p. 091302.
- [19] Bruno Pontecorvo. ‘Mesonium and antimesonium’. In: *Zhur. Eksptl. i Teoret. Fiz.* 33 (1957).
- [20] Ziro Maki, Masami Nakagawa and Shoichi Sakata. ‘Remarks on the unified model of elementary particles’. In: *Progress of Theoretical Physics* 28.5 (1962), pp. 870–880.
- [21] Q Retal Ahmad et al. ‘Direct evidence for neutrino flavor transformation from neutral-current interactions in the Sudbury Neutrino Observatory’. In: *Physical review letters* 89.1 (2002), p. 011301.
- [22] Yoshiyuki Fukuda et al. ‘Evidence for oscillation of atmospheric neutrinos’. In: *Physical review letters* 81.8 (1998), p. 1562.
- [23] F P An et al. ‘Observation of electron-antineutrino disappearance at Daya Bay’. In: *Phys. Rev. Lett.* 108.17 (Apr. 2012), p. 171803.
- [24] K Abe et al. ‘Observation of electron neutrino appearance in a muon neutrino beam’. In: *Phys. Rev. Lett.* 112.6 (Feb. 2014), p. 061802.
- [25] N Abgrall et al. ‘The large enriched germanium experiment for neutrinoless double beta decay (LEGEND)’. In: *PROCEEDINGS OF THE INTERNATIONAL CONFERENCE OF GLOBAL NETWORK FOR INNOVATIVE TECHNOLOGY AND AWAM INTERNATIONAL CONFERENCE IN CIVIL ENGINEERING (IGNITE-AICCE17): Sustainable Technology And Practice For Infrastructure and Community Resilience* (2017).
- [26] Particle Data Group. ‘Review of particle physics’. In: *Prog. Theor. Exp. Phys.* 2022.8 (Aug. 2022).

- [27] Matteo Agostini et al. ‘Final results of GERDA on the search for neutrinoless double- $\beta$  decay’. In: *Physical review letters* 125.25 (2020), p. 252502.
- [28] Kai Zuber. *Neutrino Physics, Third Edition*. 3rd ed. Series in High Energy Physics, Cosmology and Gravitation. London, England: CRC Press, June 2019.
- [29] Valerie Domcke et al. ‘MeV-scale seesaw and leptogenesis’. In: *Journal of High Energy Physics* 2021.1 (2021), pp. 1–19.
- [30] T Yanagida. ‘Horizontal Symmetry and Masses of Neutrinos’. In: *Prog. Theor. Phys.* 64.3 (Sept. 1980), pp. 1103–1105.
- [31] Elcio Abdalla et al. ‘Cosmology intertwined: A review of the particle physics, astrophysics, and cosmology associated with the cosmological tensions and anomalies’. In: (Mar. 2022). arXiv: 2203.06142 [astro-ph.CO].
- [32] Douglas Clowe et al. ‘A direct empirical proof of the existence of dark matter’. In: *The Astrophysical Journal* 648.2 (2006), p. L109.
- [33] A. Aguilar et al. ‘Evidence for neutrino oscillations from the observation of  $\bar{\nu}_e$  appearance in a  $\bar{\nu}_\mu$  beam’. In: *Phys. Rev. D* 64 (11 Nov. 2001), p. 112007. DOI: 10.1103/PhysRevD.64.112007.
- [34] A. A. Aguilar-Arevalo et al. ‘Significant Excess of Electronlike Events in the MiniBooNE Short-Baseline Neutrino Experiment’. In: *Phys. Rev. Lett.* 121 (22 Nov. 2018), p. 221801. DOI: 10.1103/PhysRevLett.121.221801.
- [35] W Hampel et al. ‘Final results of the  $^{51}\text{Cr}$  neutrino source experiments in GALLEX’. en. In: *Phys. Lett. B* 420.1-2 (Feb. 1998), pp. 114–126.
- [36] V V Barinov et al. ‘Results from the Baksan Experiment on Sterile Transitions (BEST)’. en. In: *Phys. Rev. Lett.* 128.23 (June 2022), p. 232501.
- [37] M Aker et al. ‘Improved eV-scale sterile-neutrino constraints from the second KATRIN measurement campaign’. In: *Physical Review D* 105.7 (2022), p. 072004.
- [38] F Bezrukov. ‘ $\nu$ MSSM and its experimental tests’. In: *Journal of Physics: Conference Series*. Vol. 110. 8. IOP Publishing. 2008, p. 082002.
- [39] Kevork Abazajian, George M Fuller and Mitesh Patel. ‘Sterile neutrino hot, warm, and cold dark matter’. In: *Physical Review D* 64.2 (2001), p. 023501.
- [40] Esra Bulbul et al. ‘Searching for the 3.5 keV Line in the Stacked Suzaku Observations of Galaxy Clusters’. In: *Astrophys. J.* 831.1 (Oct. 2016), p. 55.
- [41] Nico Cappelluti et al. ‘Searching for the 3.5 keV line in the deep fields with Chandra: The 10 ms observations’. In: *Astrophys. J.* 854.2 (Feb. 2018), p. 179.
- [42] S Bhargava et al. ‘The XMM Cluster Survey: new evidence for the 3.5-keV feature in clusters is inconsistent with a dark matter origin’. en. In: *Mon. Not. R. Astron. Soc.* 497.1 (Sept. 2020), pp. 656–671.

- [43] Katrin Collaboration. ‘KATRIN Design Report’. In: *FZKA report 7090* (2005).
- [44] Christian Karl and Susanne Mertens. *Analysis of first tritium data of the KATRIN experiment*. Master’s Thesis. Technical University of Munich, 2018.
- [45] Karen Hugenberg. *Design of the electrode system for the KATRIN main spectrometer*. Diploma thesis. WWU Münster, 2008.
- [46] M Aker et al. ‘The design, construction, and commissioning of the KATRIN experiment’. In: *Journal of Instrumentation* 16.08 (2021), T08015.
- [47] Martin Descher. ‘Differential spectrum modeling and sensitivity for keV sterile neutrino search at KATRIN’. PhD thesis. Karlsruher Institut für Technologie (KIT), 2024.
- [48] M Aker et al. ‘Precision measurement of the electron energy-loss function in tritium and deuterium gas for the KATRIN experiment’. In: *Eur. Phys. J. C Part. Fields* 81.7 (July 2021).
- [49] Daniel Furse et al. ‘Kassiopeia: a modern, extensible C++ particle tracking package’. In: *New Journal of Physics* 19.5 (2017), p. 053012.
- [50] M Aker et al. ‘Search for keV-scale sterile neutrinos with the first KATRIN data’. In: *Eur. Phys. J. C Part. Fields* 83.8 (Aug. 2023).
- [51] S Mertens et al. ‘Sensitivity of next-generation tritium beta-decay experiments for keV-scale sterile neutrinos’. In: *Journal of Cosmology and Astroparticle Physics* 2015.02 (2015), p. 20.
- [52] Anthony Onillon. ‘Neutrino mass measurement and sterile neutrinos search with the KATRIN experiment’. In: *EPJ Web of Conferences*. Vol. 282. EDP Sciences. 2023, p. 01011.
- [53] Susanne Mertens et al. ‘A novel detector system for KATRIN to search for keV-scale sterile neutrinos’. In: *J. Phys. G Nucl. Part. Phys.* 46.6 (June 2019), p. 065203.
- [54] JF Amsbaugh et al. ‘Focal-plane detector system for the KATRIN experiment’. In: *Nuclear Instruments and Methods in Physics Research Section A: Accelerators, Spectrometers, Detectors and Associated Equipment* 778 (2015), pp. 40–60.
- [55] Anton Huber. ‘Analysis of first KATRIN data and searches for keV-scale sterile neutrinos’. PhD thesis. Karlsruhe Institute of Technology (KIT), 2021.
- [56] Pia Voigt and Susanne Mertens. *Transmission properties of the KATRIN main spectrometer (when operated) for a keV-scale sterile neutrino search*. Master’s Thesis. Technical University of Munich, 2023.

- [57] Peter Lechner et al. ‘Silicon drift detectors for high resolution room temperature X-ray spectroscopy’. In: *Nuclear Instruments and Methods in Physics Research Section A: Accelerators, Spectrometers, Detectors and Associated Equipment* 377.2-3 (1996), pp. 346–351.
- [58] Christina Bruch and Susanne Mertens. *Characterisation of a 166-Pixel TRISTAN Detector Module in the KATRIN Monitor Spectrometer*. Master’s Thesis. Technical University of Munich, 2023.
- [59] C J Martoff et al. ‘HUNTER: precision massive-neutrino search based on a laser cooled atomic source’. In: *Quantum Science and Technology* 6.2 (Feb. 2021), p. 024008. DOI: 10.1088/2058-9565/abdb9b.
- [60] Anthony Onillon. *keV sterile neutrino search with the KATRIN experiment*. NuMass Conference. 2024. URL: [https://agenda.infn.it/event/38742/contributions/223211/attachments/116813/168496/NuMASS\\_2024\\_keVsterile\\_ONILLON.pdf](https://agenda.infn.it/event/38742/contributions/223211/attachments/116813/168496/NuMASS_2024_keVsterile_ONILLON.pdf).
- [61] G. Neubert and S. Rogaschweski. ‘Backscattering Coefficient Measurements of 15 to 60 keV Electrons for Solids at Various Angles of Incidence’. In: *Massenspektrometrie, Bereich Angewandte, phys. stat. sol.(a)* 59 (1980), p. 35.
- [62] Daniela Spreng and Susanne Mertens. *Electron Backscattering on Silicon Drift Detectors and Its Impact on a Sterile Neutrino Search with KATRIN*. Master’s Thesis. Technical University of Munich, 2023.
- [63] Christian Forstner and Susanne Mertens. *Characterization of a TRISTAN Silicon Drift Detector Array with a Laser System*. Master’s Thesis. Technical University of Munich, 2023.
- [64] Martin Descher et al. *TRModel*. KATRIN Software. 2023. URL: <https://nuserv.uni-muenster.de:8443/katrin-git/tristan/trmodel>.
- [65] John Allison et al. ‘Recent developments in Geant4’. In: *Nuclear instruments and methods in physics research section A: Accelerators, Spectrometers, Detectors and Associated Equipment* 835 (2016), pp. 186–225.
- [66] M. Slezak, A. Lokhov and N. Trost. *Tristan Source Sim*. KATRIN Software. 2019. URL: <https://nuserv.uni-muenster.de:8443/katrin-git/tristan/TristanSourceSim>.
- [67] SN Ketkar and M Fink. ‘Effect of Vibration in Electron Scattering by H<sub>2</sub> and D<sub>2</sub>’. In: *Physical Review Letters* 45.19 (1980), p. 1551.
- [68] Stefan Groh. ‘Modeling of the response function and measurement of transmission properties of the KATRIN experiment’. PhD thesis. Karlsruhe Institute of Technology (KIT), 2015.

- [69] Hans Bethe. ‘Zur Theorie des Durchgangs schneller Korpuskularstrahlen durch Materie’. In: *Annalen der Physik* 397.3 (1930), pp. 325–400.
- [70] Amr El Miniawy and Alejandro Saenz. *On the Karlsruhe Tritium Neutrino Experiment Energy-Loss Function*. Bachelor’s Thesis. Humboldt-Universität zu Berlin, 2021.
- [71] J W Liu. ‘Total cross sections for high-energy electron scattering by  $H_2$  ( $1 \Sigma g+$ ),  $N_2$  ( $1 \Sigma g+$ ), and  $O_2$  ( $3 \Sigma g-$ )’. In: *Physical Review A* 35.2 (1987), p. 591.
- [72] R C Ulsh, H F Wellenstein and R A Bonham. ‘Bethe surface, elastic and inelastic differential cross sections, Compton profile, and binding effects for  $H_2$  obtained by electron scattering with 25 keV incident electrons,’ in: *J. Chem. Phys.*, v. 60, no. 1, pp. 103-111 (Jan. 1974). URL: <https://www.osti.gov/biblio/4354673>.
- [73] *Hydrogen*. NIST Chemistry WebBook, SRD 69. URL: <https://webbook.nist.gov/cgi/cbook.cgi?ID=C1333740&Mask=20>.
- [74] J W Liu. ‘Total Inelastic Cross section for Collisions of  $H_2$  with Fast Charged Particles’. In: *Physical Review A* 7.1 (1973), p. 103.
- [75] Włodzimierz Kołos, Hendrik J Monkhorst and Krzysztof Szalewicz. ‘Energy unresolved differential cross section for electron scattering by  $H_2$ ’. In: *The Journal of Chemical Physics* 77.3 (1982), pp. 1323–1334.
- [76] S P Khare and B L Moiseiwitsch. ‘The angular distribution of electrons elastically scattered by helium atoms and by hydrogen molecules’. In: *Proc. Phys. Soc.* 85.5 (May 1965), pp. 821–839.
- [77] Jacek Komasa and Ajit J Thakkar. ‘Small-angle elastic scattering of high-energy electrons by  $H_2$ ,  $HD$ , and  $D_2$ ’. In: *Physical Review A* 49.2 (1994), p. 965.
- [78] Yuheng Zhang, Andrew W Ross and Manfred Fink. ‘High-energy electron scattering study of molecular hydrogen’. In: *Physical Review A* 43.7 (1991), p. 3548.
- [79] Ferenc Glück. *Angular differential cross section for  $e-H$  and  $eH_2$  electronic excitation scattering*. Karlsruhe Institute of Technology, Unpublished Report. 2023.
- [80] G P Arrighini, F Biondi and C Guidotti. ‘A study of the inelastic scattering of fast electrons from molecular hydrogen’. In: *Molecular Physics* 41.6 (1980), pp. 1501–1514.
- [81] N. F. Mott and H. S. W. Massey. *The Theory of Atomic Collisions*. London: Oxford University Press, 1965.

- [82] Ferenc Glück. *Secondary Electron Distribution in e-H ionization scattering*. Karlsruhe Institute of Technology, Unpublished Report. 2024.
- [83] M Eugene Rudd. ‘Differential and total cross sections for ionization of helium and hydrogen by electrons’. In: *Physical Review A* 44.3 (1991), p. 1644.
- [84] RR Goruganthu and RA Bonham. ‘Secondary-electron-production cross sections for electron-impact ionization of helium’. In: *Physical Review A* 34.1 (1986), p. 103.
- [85] R Muller-Fiedler, K Jung and H Ehrhardt. ‘Double differential cross sections for electron impact ionisation of helium’. In: *Journal of Physics B: Atomic and Molecular Physics* 19.8 (1986), p. 1211.
- [86] Donald Rapp and Paula Englander-Golden. ‘Total cross sections for ionization and attachment in gases by electron impact. I. Positive ionization’. In: *The Journal of Chemical Physics* 43.5 (1965), pp. 1464–1479.
- [87] B Van Wingerden, RW Wagenaar and FJ De Heer. ‘Total cross sections for electron scattering by molecular hydrogen’. In: *Journal of Physics B: Atomic and Molecular Physics* 13.17 (1980), p. 3481.
- [88] Nobuo Oda. ‘Energy and angular distributions of electrons from atoms and molecules by electron impact’. In: *Radiation Research* 64.1 (1975), pp. 80–95.
- [89] Rudolf Sack. ‘Measurement of the energy loss of 18.6 keV electrons on deuterium gas and determination of the tritium Q-value at the KATRIN experiment’. PhD thesis. Westfaelische Wilhelms-Universitaet Muenster, 2020.
- [90] Yong-Ki Kim and M Eugene Rudd. ‘Binary-encounter-dipole model for electron-impact ionization’. In: *Physical Review A* 50.5 (1994), p. 3954.
- [91] Frederick James. ‘Monte Carlo theory and practice’. In: *Reports on progress in Physics* 43.9 (1980), p. 1145.
- [92] David JC MacKay. *Information theory, inference and learning algorithms*. Cambridge university press, 2003.
- [93] Rubin H Landau, Manuel José Páez Mejia and Cristian C Bordeianu. *A survey of computational physics: introductory computational science*. Princeton University Press, 2008.
- [94] Makoto Matsumoto and Takuji Nishimura. ‘Mersenne twister: a 623-dimensionally equidistributed uniform pseudo-random number generator’. In: *ACM Transactions on Modeling and Computer Simulation (TOMACS)* 8.1 (1998), pp. 3–30.
- [95] Luc Devroye. *Non-Uniform Random Variate Generation*. New York: Springer Verlag, 1986.

- [96] Pierre Brémaud. *Markov Chains*. New York: Springer Verlag, 1999.
- [97] L. D. Landau and E. M. Lifshitz. *Mechanics*. Oxford: Butterworth-Heinenann, 1960.
- [98] Anthony Onillon. *Source scattering simulation - First comparison between MC code and convolution code results*. Technical University of Munich, Unpublished Report. 2024.
- [99] Richard Salomon. *Private Communication*. 2024.